Combustion and Flame 183 (2017) 224–241

Contents lists available at ScienceDirect

Combustion and Flame

journal homepage: www.elsevier.com/locate/combustflame

Feature Article

Sensitivity of predictions to chemical kinetics models in a temporally evolving turbulent non-premixed flame

Suo Yang, Reetesh Ranjan, Vigor Yang, Wenting Sun*, Suresh Menon*

School of Aerospace Engineering, Georgia Institute of Technology, Atlanta, GA 30332, USA

ARTICLE INFO

Article history:
Received 18 November 2016
Revised 14 May 2017
Accepted 14 May 2017

Keywords:
Turbulent flames
Extinction and re-ignition
Chemical kinetics
Finite-rate effects

ABSTRACT

To investigate the sensitivity of predictions to chemical kinetics models, two different kinetics models, GRI-Mech 3.0 and an 11-species syngas model, are compared by performing 3D finite-rate kinetics-based direct numerical simulations (DNS) of a temporally evolving turbulent non-premixed syngas flame. Dynamic adaptive chemistry and correlated transport techniques are applied to enable computationally efficient simulation with the detailed GRI-Mech 3.0. Both chemical kinetics models, providing comparable qualitative trends, capture local extinction and re-ignition events. However, significant quantitative discrepancies (86–100 K difference in the temperature field) indicate high sensitivity to the chemical kinetics model. The 11-species model predicts a lower radicals-to-products conversion rate, causing statistically more local extinction and less re-ignition. This sensitivity to the chemical kinetics model is magnified relative to a 1D steady laminar simulation by the effects of unsteadiness and turbulence (up to 7 times for temperature, up to 12 times for CO, up to 13 times for H_2, up to 7 times for O_2, up to 5 times for CO_2, and up to 13 times for H_2O), with the deviations in species concentrations, temperature, and reaction rates forming a nonlinear positive feedback loop under reacting flow conditions. The differences between the results from the two models are primarily due to: (a) the larger number of species and related kinetic pathways in GRI-Mech 3.0; and (b) the differences in reaction rate coefficients for the same reactions in the two models. Both (a) and (b) are sensitive to unsteadiness and other turbulence effects, but (b) is dominant and is more sensitive to unsteadiness and other turbulence effects. At local extinction, the major differences between the results from the two chemical kinetics models are in the peak values and the volume occupied by the peak values, which is dominated by unsteady effects; at re-ignition, the differences are mainly observed in the spatial distribution of the reacting flow field, which is primarily dominated by the complex turbulence–chemistry interaction.

1. Introduction

Direct numerical simulation (DNS) and large eddy simulation (LES) are powerful tools for understanding the complex interplay of turbulent mixing, molecular diffusion, and finite-rate kinetics. These approaches are critical to analyzing and improving the design and development of advanced energy conversion and propulsion systems. However, DNS/LES suffers from a bottleneck in the calculation of the stiff finite-rate chemical reactions and transport properties, when moderately complex to detailed chemical kinetics models are employed to account for a wide range of combustion processes. Furthermore, it is unclear how different chemical kinetics models affect DNS/LES results on local extinction and re-ignition phenomena in turbulent combustion environments. These events may lead to increased emissions, combustion instability, or flame blowout, however; so accurate prediction of them is an important aspect of high-fidelity simulations. Accurate prediction will in turn require a quantitative understanding of the wide range of time and length scales involved, and of the complex interactions between turbulent mixing, molecular diffusion, and chemical reactions.

Detailed finite-rate chemistry and mixture-averaged transport are computationally intensive, especially in 3D turbulent combustion simulations [1–3]. For this reason, except for those consuming excessive computational resources and time [4–6], most past DNS/LES studies of turbulent combustion have used either a flamelet model with detailed chemistry (∼50 species or more) [7–10] or a simplified/reduced finite-rate chemical kinetics model with non-stiff reactions (∼10 species) [11–16]. Both approaches, however, are of limited accuracy and may reduce the overall quality of prediction [17]. Therefore, acceleration of the computation

---

* Corresponding authors.
E-mail addresses: wenting.sun@aerospace.gatech.edu, jedibill2010@gmail.com (W. Sun), suresh.menon@aerospace.gatech.edu (S. Menon).

http://dx.doi.org/10.1016/j.combustflame.2017.05.016

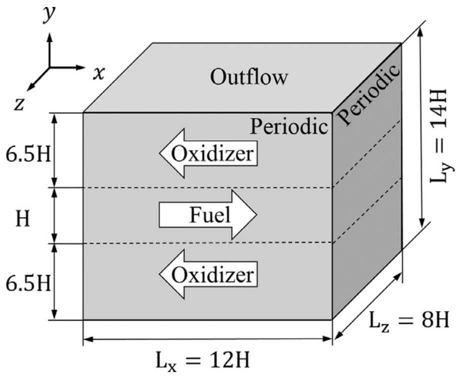

Fig. 1. Schematic of the canonical temporally evolving non-premixed flame.

of chemical kinetics and transport properties will be required to enable computationally efficient and accurate simulations with the DNS/LES approach employing detailed finite-rate chemical kinetics models.

In order to reduce computational cost, several mechanism reduction methods [18–21] have been proposed. These models essentially reduce the number of species in the chemical kinetics models. Well-verified by homogeneous ignition delays, extinction curves in the perfectly stirred reactor, and laminar flame speeds, globally reduced models for hydrocarbons generally require at least ~40 species to cover all user-defined conditions of interest (fuel type, oxidizer type, equivalence ratio, initial pressure and temperature). Unfortunately, such a large number of species is still too large for DNS/LES using the finite-rate kinetics approach. To tackle this challenge, dynamic adaptive chemistry (DAC) [22,23] was proposed to utilize detailed stiff finite-rate chemistry. DAC generates locally-optimized reduced kinetics for each spatial location and time step, and only the reaction rates of active species are calculated. DAC has been applied to accelerate the kinetics computation in DNS of 0D/1D reactors [24], 2D RANS of DI engines [25], and 3D URANS and LES of spray flames [26]. To further reduce the large computational overhead of DAC in mechanism reduction, Correlated-DAC (CO-DAC) [27] and Correlated-DAC & Transport (CO-DACT) [28] were introduced to further accelerate both chemistry and transport calculation in 0D/1D simulation of laminar flames. Recently, Yang et al. rigorously verified and optimized CO-DACT in DNS of a turbulent premixed flame in the thin reaction zone regime [29], and in LES of a turbulent partially premixed flame [30], to allow computationally efficient DNS/LES with detailed finite-rate chemistry. The sensitivity of simulation results to different chemical kinetics models is still unclear, however, particularly with regard to the prediction of local extinction and re-ignition events. This is the focus of the present investigation.

Most existing chemical kinetics models offer similar predictions of ignition and extinction in 0D/1D finite-rate simulations of laminar combustion processes. Is it appropriate, therefore, to extend this observation to a 3D turbulent combustion environment? This question is practically important because most large-scale combustion simulations were conducted using (globally reduced) chemical kinetics models validated/verified purely based on 0D/1D steady laminar tests. In order to answer this question, two different chemical kinetics models (GRI-Mech 3.0 [31] and an 11-species model [13]) are used to simulate a temporally evolving turbulent non-premixed syngas flame, and the results are compared.

2. Physical model and flow conditions

In this study, we consider a canonical temporally-evolving non-premixed flame (shown in Fig. 1). This type of flame has been extensively studied in the past, using DNS [12,13,15] and LES [14,16]. The flow parameters and the grid information are provided in Table 1. We consider a reduced characteristic jet velocity $U = 100\,\mathrm{m/s}$ to allow for simulations with a coarse grid. All the simulations are conducted at pressure $P = 1\,\mathrm{atm}$. The canonical flow configuration comprises an inner fuel jet (50% CO, 10% H_2, and 40% N_2 by volume) and an outer oxidizer stream (25% O_2 and 75% N_2 by volume), which are counter-flowing in the streamwise direction. The jet has a Reynolds number (Re_{jet}) of 2315 and a Damkohler number (Da) of 0.01, which is low enough to induce local extinction during turbulence–chemistry interaction and evolution. The extent of the computational domain is $L_x \times L_y \times L_z \equiv 12H \times 14H \times 8H$, where $H = 0.96\,\mathrm{mm}$ is the initial width of the fuel jet. The simulations in this study employ about 18 uniformly spaced points along H, which leads to approximately 2.1 M grid points total, with a minimum resolution of approximately 4η, where η is the Kolmogorov length-scale. A past DNS study [13] reports that η grows with time and becomes comparable to the grid size Δx; the grid resolution considered in this study is therefore adequate to capture the extinction and re-ignition dynamics. A grid convergence test is included in Fig. S1 of the Supplementary material, to show that the observations in this study are insensitive to grid resolution.

The reacting flow field is initialized with a laminar flamelet solution [32] at a bulk strain rate $\kappa = 0.75\kappa_q$, where $\kappa_q = 1295\ \mathrm{s}^{-1}$ is the extinction bulk strain rate. Here, κ_q is obtained by gradually increasing the bulk strain rate in the laminar flamelet calculation until extinction occurs. To allow for the evolution of shear layer turbulence, broadband isotropic turbulence is superimposed on the mean flow with an initial integral length-scale of $H/3$, and turbulence intensity of $0.05U$. A perfectly non-reflecting, characteristic-based outflow boundary condition is used in the transverse (y) direction, whereas a periodic boundary condition is specified along the streamwise (x) and spanwise (z) directions. The characteristic transient jet time is defined as $t_j = H/U$, and the simulations are conducted up to $40\,t_j$ to capture both the extinction and re-ignition events.

3. Numerical methodology

3.1. Compressible reacting flow solver

In this study, the well-established reacting flow solver AVF-LESLIE [33,34] was used. It is a multi-physics and multi-species compressible flow solver for DNS/LES of non-reacting/reacting flows in canonical and moderately complex flow configurations. It has been extensively used in the past to investigate a wide range of combustion problems, including acoustic flame-vortex interactions, premixed flame turbulence interactions, and scalar mixing [34–36]. The solver uses the 2nd-order accurate MacCormack finite volume scheme [37] on generalized curvilinear coordinates, and an explicit 2nd-order accurate scheme for time-integration. A fractional-step method [38,39] is used to treat the convection-diffusion term and

Table 1
Simulation case.

	Mach	Re_{jet}	Da	η (m)	Δx (m)	Grid points
Simulation case	0.11	2315	0.01	1.2×10^{-5}	5.25×10^{-5}	$128 \times 256 \times 64$

the kinetics source term separately. The solver can handle arbitrarily complex finite-rate chemical kinetics, where the thermodynamic properties are computed based on a thermally perfect gas assumption, and the transport properties are computed using a mixture-averaged formulation. The solver has been demonstrated in large-scale turbulent combustion simulations on HPC platforms exhibiting strongly scalable parallel performance [29,40]. Our tests show that the simulation results are not affected by HPC architecture, processor counts, and processors topology obtained from MPI domain decomposition.

3.2. Chemical kinetics models

Two chemical kinetics models are compared in this study. The first model, GRI-Mech 3.0 [31], comprises 325 steps and 53 species, and serves as a detailed stiff mechanism for syngas. The second is a 21-step, 11-species non-stiff mechanism [13] developed by Hawkes et al., which has been used in past DNS [13] and LES [14,16] studies. Predictions of the extinction strain rates and the laminar flame speeds by the 11-species model are within 1% and 5%, respectively, of those from GRI-Mech 3.0 (as shown in Table S1 and Fig. S2 of the Supplementary material). The two kinetics models predict very close adiabatic flame temperatures (~12 K difference). Further examination of the 11-species model and GRI-Mech 3.0 shows that most reaction rate coefficients for the same reactions are different for these two models. It should be emphasized that the 11-species model is independent of GRI-Mech 3.0. Since the transport data for these models are identical, any difference in simulation results must come from differences in the chemical reactions.

3.3. ODE solvers

There are generally 3 categories of ODE solvers available for the calculation of chemical kinetics: (1) pure implicit solvers, such as the variable-coefficient stiff ODE solver (VODE) [41]; (2) semi-implicit solvers, such as the point-implicit stiff ODE solver (ODEPIM) [42,43]; and (3) pure explicit solvers, such as the 4th-order Runge–Kutta (RK4) solver and Euler explicit solver with sub-cycling. Pure implicit solvers, although accurate even for stiff mechanisms, are computationally expensive. For example, VODE is more than 40 times slower than ODEPIM while employing GRI-Mech 3.0. Pure explicit solvers require time step sizes smaller than the smallest chemical timescales; otherwise significant errors or even numerical instability may be triggered. For the present evolving non-premixed flame using stiff mechanisms (such as GRI-Mech 3.0), the minimum chemical timescales are O(0.1 ns), while the time step sizes from the CFL condition are O(10 ns). Numerical experiments show that using RK4 for stiff mechanisms can introduce significant errors and incorrect results; for example, the average temperature error was more than 400 K in our investigation. For reasons of both accuracy and computational speed, therefore, ODEPIM is selected in this study.

3.4. Dynamic adaptive chemistry (DAC)

DAC generates locally-reduced kinetics for each spatial location and time step by the path flux analysis method [20]. Only the instantaneous reaction rates of active species are calculated based on the Arrhenius law as functions of the instantaneous gas temperature and composition. The transport equations for the inactive species are solved to guarantee the conservation of species, but their chemical source terms are set to zero to reduce the computational cost of chemical kinetics. To reduce the computational overhead for mechanism reduction, a correlation technique [27,29,30,44] is introduced to share the reduced kinetics among time-space points with similar thermochemical states.

3.5. Correlated transport (CoTran)

Mixture-averaged transport coefficients are employed for the computation of viscous, thermally conductive, and species diffusion fluxes, and to capture differential diffusion and the strong interaction among molecular diffusion, turbulent mixing, and finite-rate kinetics. Using the same correlation technique as in DAC but different grouping criteria [28–30,44], the calculation of mixture-averaged transport coefficients can be reduced significantly without computational overhead. DAC and CoTran are discussed in detail in Refs. [29,30,44].

4. Results and discussion

4.1. Instantaneous reacting flow features

The contours of the OH mass fraction in Fig. 2(a and b) illustrate the spatial evolution of the flame structure during the local extinction and re-ignition process. The flame location is identified using the stoichiometric mixture fraction iso-lines. Mixture fraction Z is defined as

$$Z = \left[\frac{sY_F - Y_O + Y_{O,0}}{sY_{F,0} + Y_{O,0}} \right], \tag{1}$$

where $s = AFR_{stoich} = (W_O \times \nu_O)/(W_F \times \nu_F)$, with $Y_{F,\,0}$ being the fuel mass fraction at the fuel stream inlet, $Y_{O,\,0}$ denoting the oxidizer mass fraction at the oxidizer stream inlet, and Y_O denoting the local oxidizer mass fraction. Here, W_F and W_O are the species molecular weights, and ν_F and ν_O are the fuel and oxygen stoichiometric coefficients, respectively.

At $20\,t_j$, only few discrete OH pockets survive and attach to the stoichiometric surfaces, indicating that local extinction is approached in most regions of the shear layers. However, at $40\,t_j$, the values of OH mass fraction increase sharply in most regions around the stoichiometric surfaces within the shear layers, indicating the approach of re-ignition. Some of the disconnected small radical pockets observed at $20\,t_j$ become the source of re-ignition at $40\,t_j$. The transverse movement of the flame occurs due to the spatial evolution of the shear layers in the transverse direction with time. This is apparent from Fig. 2(c and d), where the contours of the vorticity magnitude qualitatively illustrate the transverse spreading of the shear layers. Due to this spreading, we observe dominant large-scale structures at $40\,t_j$ as compared to $20\,t_j$, with reduced peak values of vorticity magnitude.

4.2. Assessment of accuracy

DAC and CoTran have been rigorously verified in the past by simulating 0D/1D laminar flames [27,28], a turbulent premixed flame [29], and a turbulent partially premixed flame [30]. In the present study, the accuracy of DAC and CoTran is verified for a turbulent non-premixed flame. Figure 3 shows a comparison of the benchmark (using ODEPIM) and DAC+CoTran ('New') at the centerline of the computational domain under local extinction ($20\,t_j$) for temperature, vorticity magnitude, mass fraction, and reaction rate of OH. There are no observable differences in the quantities under comparison. The same results were confirmed by comparison of the 2D contours, which are omitted here for the sake of brevity. To further quantify errors, we define the absolute L^2 error as:

$$\epsilon_{abs} = \frac{1}{V}\sqrt{\int \left(Y_k^{New} - Y_k^{Benchmark}\right)^2 dV}, \tag{2}$$

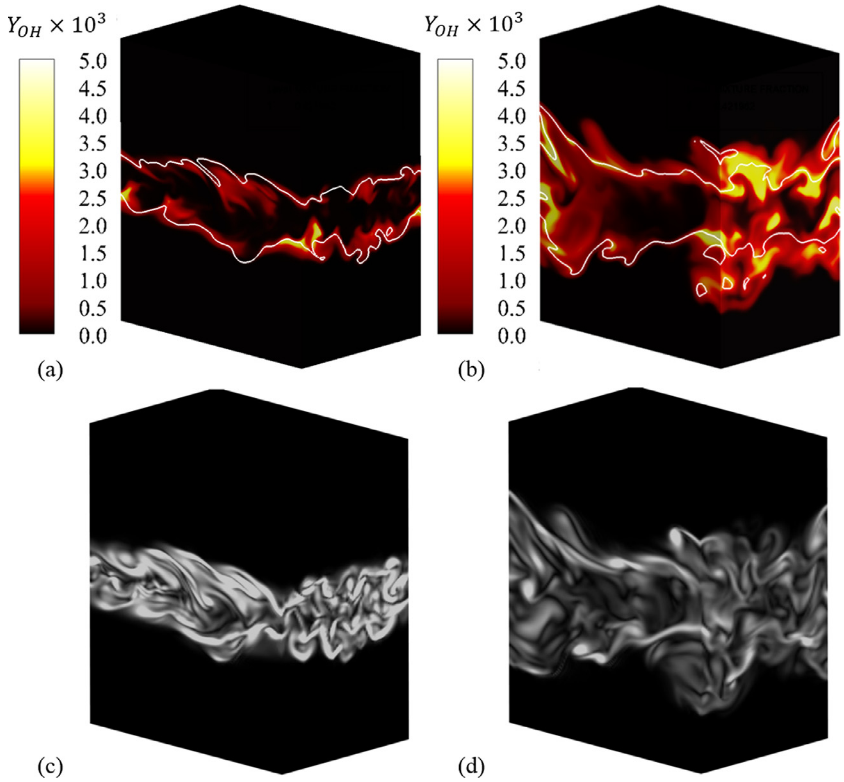

Fig. 2. Contours of OH mass fraction overlaid with stoichiometric mixture fraction (upper) and vorticity magnitude (lower) in 3D computational domain at local extinction ($20\,t_j$, left) and re-ignition ($40\,t_j$, right) from GRI-Mech 3.0.

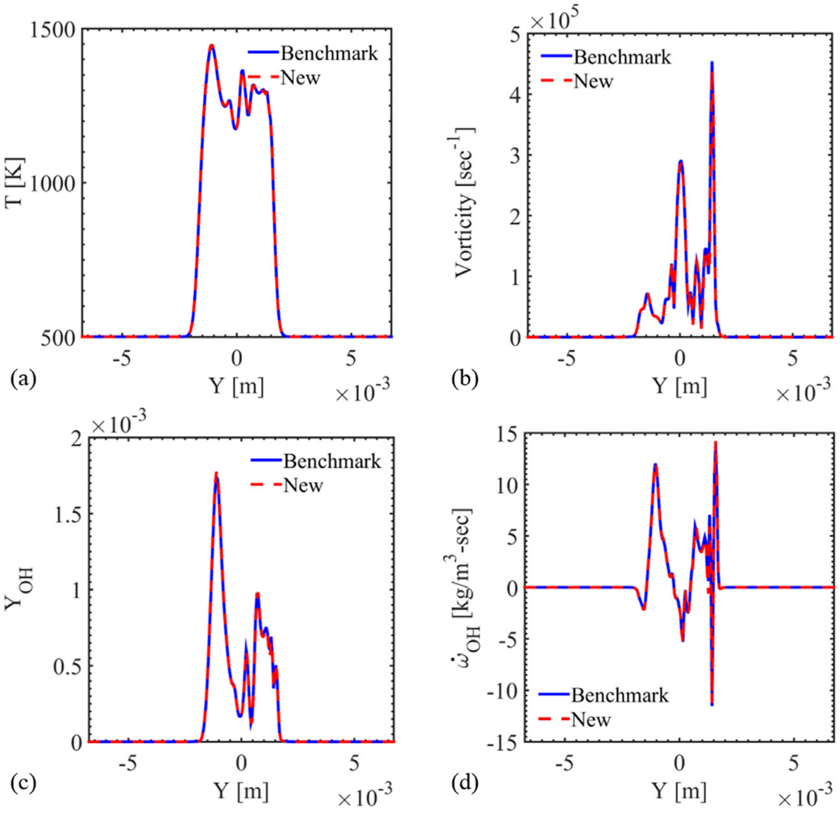

Fig. 3. Comparison of benchmark and DAC+CoTran (‘New’) at centerline of computational domain under local extinction ($20\,t_j$) for (a) temperature, (b) vorticity magnitude, (c) mass fraction of OH, and (d) reaction rate of OH.

Table 2
Errors of DAC and CoTran at local extinction ($20\,t_j$) and Re-ignition ($40\,t_j$).

Error	T (K)	Vor. (s^{-1})	Y_{CO}	Y_{H_2}	Y_{O_2}	Y_H	Y_O	Y_{OH}	Y_{CO_2}	Y_{H_2O}
ϵ_{abs}: $20\,t_j$	0.003	1.70	1.68×10^{-6}	1.22×10^{-8}	7.64×10^{-7}	2.24×10^{-9}	2.27×10^{-8}	1.04×10^{-8}	7.73×10^{-7}	1.08×10^{-7}
ϵ_{abs}: $40\,t_j$	0.021	4.65	5.38×10^{-6}	2.61×10^{-8}	4.72×10^{-6}	1.04×10^{-8}	1.87×10^{-7}	7.84×10^{-8}	5.22×10^{-6}	3.68×10^{-7}
ϵ_{rel}(%): $20\,t_j$	0.66	3.93	1.48	1.49	0.47	1.79	3.46	3.78	2.05	1.46
ϵ_{rel}(%): $40\,t_j$	2.87	15.76	6.14	5.64	3.29	4.79	11.23	9.69	6.18	3.99

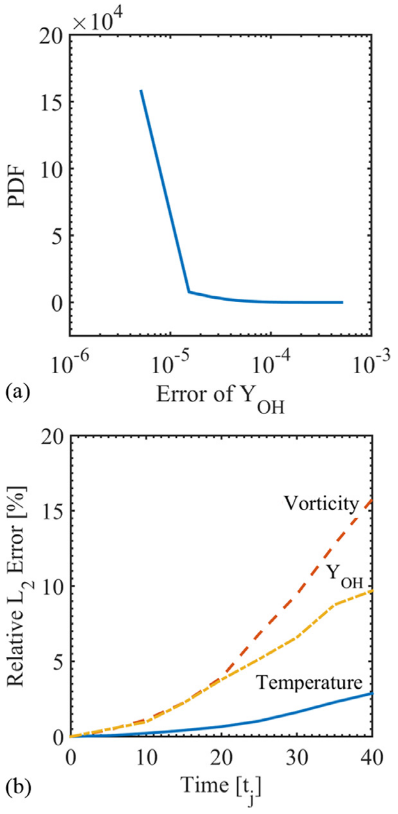

Fig. 4. (a) PDF of mass fraction errors of OH under local extinction ($20\,t_j$), and (b) temporal evolution of relative L^2 errors of temperature, vorticity magnitude, and mass fraction of OH through 3D computational domain for DAC+CoTran.

and the relative L^2 error as:

$$\epsilon_{rel} = \sqrt{\frac{\int \left(Y_k^{New} - Y_k^{Benchmark}\right)^2 dV}{\int \left(Y_k^{Benchmark}\right)^2 dV}}. \tag{3}$$

These metrics provide the most stringent test, since local point-wise errors can be made even if the benchmark and the new method have similar means and PDFs. The PDF of errors of Y_{OH} at local extinction ($20\,t_j$), and the temporal evolution of relative errors of temperature, vorticity magnitude, and Y_{OH}, are presented in Fig. 4. The error distribution is highly concentrated at its mean value near zero, and large errors are rare events. There is some error accumulation for all quantities, but it is slow considering the long run time of $40\,t_j$. In addition, the error of temperature grows much slower than that of Y_{OH} and vorticity magnitude. Table 2 shows the quantified errors of DAC+CoTran at local extinction ($20\,t_j$) and re-ignition ($40\,t_j$) for temperature, vorticity magnitude, and mass fraction of representative species. The error is small even at the end of the simulation, especially for temperature (0.02 K) and major species (within 6%). In summary, DAC+CoTran provides an accurate prediction of the 3D turbulent non-premixed flame.

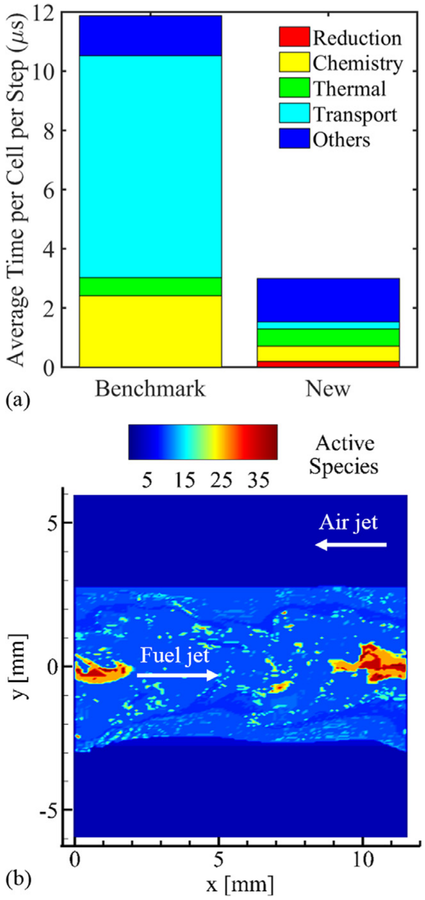

Fig. 5. (a) Comparison of computational time use distribution for benchmark and DAC+CoTran ('New') and (b) 2D contours of active species number at local extinction ($20\,t_j$).

4.3. Assessment of computational cost

Figure 5(a) shows the speed-up using DAC and CoTran versus the ODEPIM benchmark. Notably, DAC speeds up the calculation of chemical kinetics by 3.4 times, and CoTran speeds up the calculation of mixture-averaged transport properties by 32 times. Together, they provide a net speed-up of a factor of 4. Since ODEPIM is used for the time-integration of chemical reactions, it is the calculation of transport properties that dominates the total computational time of the benchmark simulation, and, therefore, CoTran contributes most to the net speed-up.

The speed-up from DAC depends heavily on the stiffness of the chemical kinetics models. This is apparent from Fig. 5(b), which shows the distribution of the number of active species at local extinction ($20\,t_j$). Outside the shear layers, there are no active reactions and only 3 "hibernating" species, fuels (CO and H_2) and oxygen, which are the seeds of the chemical mechanism reduction [20]. Inside the shear layers, the high temperature region has no more than 40 reactions and 10 species, while the relatively low temperature regions have a greater number of active reactions and species.

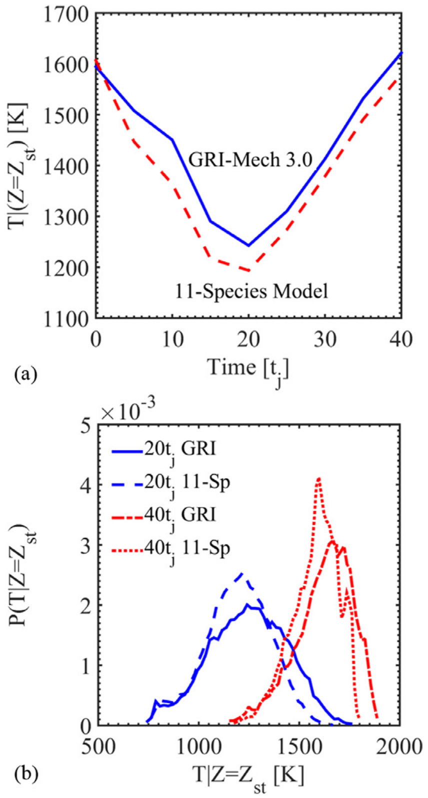

Fig. 6. (a) Temporal evolution of mean temperature on the stoichiometric surface obtained from GRI-Mech 3.0 and 11-species model; (b) PDF of temperature on the stoichiometric surface at local extinction ($20\,t_j$) and re-ignition ($40\,t_j$) from GRI-Mech 3.0 and 11-species model.

4.4. Comparison of the two kinetics models

In this section, the predictions of local extinction and re-ignition from GRI-Mech 3.0 and the 11-species model are compared through the instantaneous flame structure, conditional statistics, syngas flame structure, and scalar dissipation rate statistics. The counterparts in all the comparisons have the exact same conditions except for chemical kinetics models: the same grid, initial conditions, initial turbulence perturbation, HPC system, processor count and topology, etc. Therefore, all the differences are attributed to the chemical kinetics models.

4.4.1. Instantaneous flame structure

Figure 6 compares the temporal evolution and PDF of the temperature field on the stoichiometric surface obtained from simulations using GRI-Mech 3.0 and the 11-species model. The mean stoichiometric temperature starts at approximately 1600 K, gradually drops to 1200 K–1250 K at $20t_j$, and increases gradually to ∼1600 K at $40t_j$. This evolution of the mean temperature clearly demonstrates the approach of local extinction followed by the subsequent re-ignition. Although the starting temperature and the trend are the same, the prediction from the 11-species model gradually deviates from that of GRI-Mech 3.0. The deviation reaches its peak of 86 K (6%) near $20t_j$, but decreases slightly afterwards, stabilizes at ∼50 K, and remains stable to the end of the simulation. Temperature from the 11-species model is always lower than that from GRI-Mech 3.0, as a result of different heat release pathways/rates.

The most probable temperatures in the PDF plots follow the temporal evolution of mean temperature. PDFs at re-ignition are much narrower than those at local extinction, which indicates that even at local extinction, there are some pockets of gas in a fully burning state. The two models show a qualitatively similar structure of the PDF, but their peak values and the right tails of high temperatures are quantitatively different, as shown in Table 3. Comparing with GRI-Mech 3.0, the PDFs from the 11-species model are biased toward lower temperatures, which is consistent with the mean temperature evolution, and the standard deviation is smaller, which indicates a narrower PDF.

The initial mean temperatures in Fig. 6(a) are generated from 1D steady laminar flamelet solutions (from a counter-flow configuration), and the values are close for the two chemical kinetics models (0.76% difference), indicating that the deviation is small in 1D steady laminar flames. The deviation between the two chemical kinetics models is magnified by the unsteady turbulent configuration. Turbulence and unsteady turbulent reacting flows are chaotic dynamical systems that evolve on strange attractors of maximum dimension equal to the available degrees of freedom of the discretized system. By reducing the dimensionality of this system through elimination of governing equations, the attractor could be altered, and the chaotic system may deviate and follow a different attractor. Therefore, this is one of the potential reasons to explain the observed deviation magnification. To directly investigate the effects of chaos in this system, Fig. S3 of the Supplemental material shows the temporal evolution of mean temperature on the stoichiometric surface obtained from the 11-species model with ± 5% perturbations to the initial temperatures. In the evolution, the deviations are the same order of magnitude to the initial perturbations, with the largest deviation of ∼7% (deviation magnification), and the smallest deviation of ∼2% (deviation reduction). Therefore, there is no significant magnification of the initial perturbations. This prove that the system is insensitive to initial perturbations, and thus not a typical chaotic system. To quantitatively investigate this observation and compare with the flamelet solutions, absolute and relative mean deviations between the two chemical kinetics models (in mixture fraction space) of the 1D steady laminar flame, 3D unsteady laminar flame, and 3D turbulent flame are presented in Table 4. For an arbitrary quantity ϕ, its absolute mean deviation is defined as:

$$dev^{\phi}_{abs,\,st} = \max_{0\le t\le 40t_j} \left|\langle\phi_{GRI}|Z=Z_{st}\rangle(t) - \langle\phi_{11-sp}|Z=Z_{st}\rangle(t)\right| \tag{4}$$

and its relative mean deviation is defined as:

$$dev^{\phi}_{rel,\,st} = \max_{0\le t\le 40t_j} \left|\frac{\langle\phi_{GRI}|Z=Z_{st}\rangle(t) - \langle\phi_{11-sp}|Z=Z_{st}\rangle(t)}{\langle\phi_{GRI}|Z=Z_{st}\rangle(t)}\right| \tag{5}$$

Since the 3D turbulent flame problem is of concern here, the same configuration is used for the 3D unsteady laminar case with the initial turbulence turned off and the Reynolds number reduced to 500 to avoid the generation of turbulence from the shear layers. Due to the lower mean strain rate, local extinction does not occur in this 3D unsteady laminar flame. As shown in Table 4, the deviations increase sharply from the 1D steady laminar flame to the 3D

Table 3
Statistics of the PDF of temperature on the stoichiometric surface (Z_{st}) for the two chemical kinetics models.

Statistics	GRI-Mech 3.0 ($20\,t_j$)	11-species model ($20\,t_j$)	GRI-Mech 3.0 ($40\,t_j$)	11-species model ($40\,t_j$)
Mean	1243 K	1194 K	1622 K	1580 K
Standard deviation	194 K	163 K	141 K	115 K
Skewness	−0.15	−0.21	−0.66	−0.58

Table 4
Maximal (over time) deviations/errors of the 11-species model (11-sp), GRI-Mech 3.0 using DAC+CoTran, and GRIred11, with respect to GRI-Mech 3.0. Mean values of temperature and mass fractions of representative species on the stoichiometric surface.

Abs. deviation	T (K)	Y_{CO}	Y_{H_2}	Y_{O_2}	Y_H	Y_O	Y_{OH}	Y_{CO_2}	Y_{H_2O}
1D steady laminar: 11-sp	12.22	0.0017	0.00001	0.0012	0.000007	0.00004	0.00044	0.0025	0.0001
3D unsteady laminar: 11-sp	89.00	0.0027	0.00002	0.0019	0.000101	0.00086	0.00044	0.0045	0.0024
3D turbulent: 11-sp	86.47	0.0038	0.00010	0.0026	0.000118	0.00143	0.00033	0.0054	0.0018
3D turbulent: DAC+CoTran	01.30	0.0002	3.44E−6	0.0002	0.000003	0.00004	0.00001	0.0004	3.1E−5
1D steady laminar: GRIred11	04.03	0.0004	1.65E−6	0.0003	7.40E−07	0.00004	0.00002	0.0008	0.0001
3D turbulent: GRIred11	11.25	0.0012	0.00002	0.0008	0.000006	0.00010	0.00004	0.0013	0.0002
Rel. dev. (%)	T	Y_{CO}	Y_{H_2}	Y_{O_2}	Y_H	Y_O	Y_{OH}	Y_{CO_2}	Y_{H_2O}
1D steady laminar: 11-sp	0.76	2.07	03.69	2.08	02.03	00.69	17.77	1.18	0.51
3D unsteady laminar: 11-sp	5.18	4.80	08.64	4.82	32.82	21.62	13.24	1.65	7.77
3D turbulent: 11-sp	5.96	2.82	21.09	2.80	49.55	33.86	14.11	5.00	8.51
3D turbulent: DAC+CoTran	0.09	0.19	00.45	0.19	01.23	01.10	00.83	0.34	0.15
1D steady laminar: GRIred11	0.25	0.45	00.48	0.44	00.20	00.76	00.62	0.35	0.51
3D turbulent: GRIred11	0.91	0.77	02.01	0.77	02.88	04.02	04.10	1.38	0.90

unsteady laminar flame to the 3D turbulent flame for most quantities, including temperature and major species. In particular, the absolute deviation magnification factor is 7 for temperature, 10 for H_2, and 13 for H_2O; the relative deviation magnification factor is 8 for temperature, 6 for H_2, 4 for CO_2, and 17 for H_2O. Turbulence and other unsteady effects significantly increase the deviations between the two chemical kinetics models. The 3D unsteady laminar case is a non-chaotic system, thus chaotic system and strange attractor cannot explain the deviation magnification due to general unsteadiness effects. Similar deviation enlargement has also been observed recently in an opposing-jet laminar flame impinged with unsteady vortex [45], which is also not a chaotic system.

The shear layers undergo unsteady growth, and the complex interaction of these unsteady effects with the kinetics significantly increases the discrepancies between the two chemical kinetics models. For example, in 3D unsteady laminar simulations, the correlation coefficient of the two chemical kinetics models for the reaction rate of H_2O (defined as $\rho_{\dot{\omega}^{GRI}_{H_2O},\ \dot{\omega}^{11-sp}_{H_2O}} = \frac{cov(\dot{\omega}^{GRI}_{H_2O},\ \dot{\omega}^{11-sp}_{H_2O})}{\sigma_{\dot{\omega}^{GRI}_{H_2O}} \cdot \sigma_{\dot{\omega}^{11-sp}_{H_2O}}}$, where *cov* is the covariance, and σ_X is the standard deviation of X) is 0.96. These deviations in reaction rates, and therefore heat release rate accumulate over time, to result in the above deviations in both mass fraction and temperature.

For most quantities (except for H_2 and CO_2), the deviations between the two chemical kinetics models in the unsteady laminar case is either close to or even larger than those in the turbulent case, which means that general unsteadiness effects are more significant than turbulence effects in the mixture fraction space. Therefore, the observed deviation magnification in the turbulent case is not primarily due to the chaotic system and strange attractor. Compared to the unsteady laminar case, the addition of turbulence amplifies the deviations for some quantities, but reduces the deviations for some others. The former ones may come from different attractors in the chaotic system. However, for the latter ones, either chaos is not the dominant factor, or the altered attractor is very close to the original attractor in the chaotic system. The most important effect of turbulence is on the spatial distribution of the shear layers and mixture fraction Z, but this effect is averaged out, as shown in Table 4. Note that the error quantification is much more stringent in Table 2 than in Table 4, because large local point-wise deviations can occur even if predictions from the two chemical kinetics models have similar means and PDFs on the stoichiometric surface. Table 4 provides better error quantification of DAC+CoTran using Eqs. (4) and (5). For the prediction of all quantities, the error introduced by DAC+CoTran is only 0.09–1.23%. Both the absolute and relative errors of DAC+CoTran are one to two orders of magnitude smaller than the corresponding deviations between the results from the two chemical kinetics models. This suggests that DAC+CoTran introduces only negligible errors, which do not affect the observations discussed here.

The differences between the results using the two chemical kinetics models can be related to two major differences in the models: (a) GRI-Mech 3.0 contains 42 more species than the 11-species model, and thus contains 293 more kinetic reactions related to those 42 species, and (b) for those reactions included in both models, the reaction rate coefficients are different. To quantify the difference in the simulation results caused by the larger number of species in GRI-Mech 3.0, a globally reduced version of GRI-Mech 3.0 was created. The reduced version, which is referred to as ‘GRIred11’, only includes the 11 species treated in the 11-species model, and incorporates only those reactions related to these 11 species. Table 4 includes the deviations between detailed GRI-Mech 3.0 and GRIred11. Note that these deviations are always 2–10 times larger than the corresponding errors introduced by DAC+CoTran, which verifies that DAC is more accurate than the conventional global reduction.

Table 5 shows the contribution of (a) to the total absolute deviations between the two chemical kinetics models, and the absolute deviation magnification factors for (a), (b), and the total. The contribution of (a) is defined as the ratio of the

Table 5
Contribution from the global reduction of reaction pathways to the maximal (over time) absolute deviations between GRI-Mech 3.0 and 11-species model; absolute deviation magnification factors for (a) global reduction of reaction pathways and (b) different reaction rate coefficients, and total. Based on mean values of temperature and mass fractions of representative species on the stoichiometric surface.

Contribution from (a) to total deviation (%)	T	Y_{CO}	Y_{H_2}	Y_{O_2}	Y_H	Y_O	Y_{OH}	Y_{CO_2}	Y_{H_2O}
1D steady laminar	32.98	23.53	16.5	25.00	10.57	>100	04.55	32.00	> 100
3D turbulent	13.01	31.58	20.0	30.77	05.08	6.99	12.12	24.07	11.11
Dev. magnification factor	T	Y_{CO}	Y_{H_2}	Y_{O_2}	Y_H	Y_O	Y_{OH}	Y_{CO_2}	Y_{H_2O}
(a) Reduced pathways	2.79	3.00	12.12	2.67	08.11	002.54	2.00	1.63	0001.38
(b) Different RR coefficients	9.18	2.00	09.58	2.00	17.89	414.12	0.69	2.41	1329.36
Total	7.08	2.24	10.00	2.17	16.86	039.59	0.75	2.16	0012.55

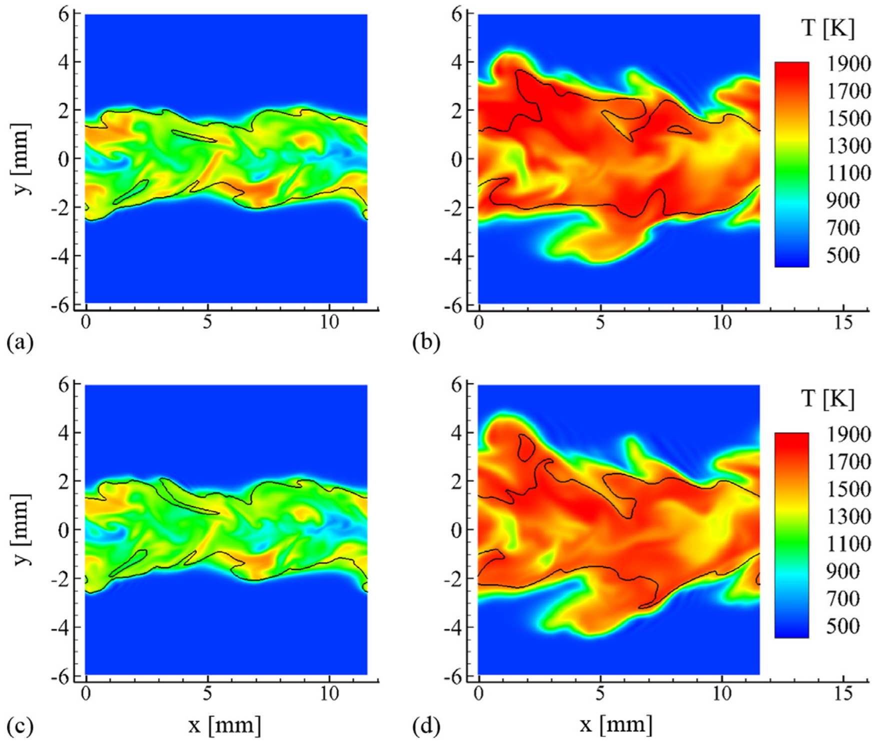

Fig. 7. Instantaneous 2D contours of temperature at 20 t_j (left) and 40 t_j (right) on center plane (Z=4H); GRI-Mech 3.0 (upper) and 11-species model (lower).

deviations between GRI-Mech 3.0 and GRIred11 to the deviations between GRI-Mech 3.0 and the 11-species model: $C^{\phi}_{(a),st} = dev^{\phi,\ (GRI\ vs\ GRIred11)}_{abs,\ st} / dev^{\phi,\ (GRI\ vs\ 11-sp)}_{abs,\ st}$. In the 1D steady laminar case, (b) dominates the total deviations for most quantities (except O and H_2O). In the 3D turbulent case, (b) dominates the total deviations for all quantities. Both (a) and (b) are sensitive to unsteadiness and other turbulence effects for all quantities, but with only (a), even though the deviation magnification is significant (up to 12 times), the relative deviations are still within ~4% for all quantities. Therefore, the global mechanism reduction is still valid for use. For temperature and all species with more than 10 times total deviation magnification (H, O, H_2O), (b) is more sensitive, which results in the rise of its contribution to total deviations from 1D steady laminar case to 3D turbulent case. In particular, for O and H_2O in the 1D steady laminar case, (a) and (b) cause deviations in opposite directions at Z_{st}. As a result, (a) contributes more than 100% deviations for O and H_2O in the 1D steady laminar case. However, the magnification factors of (b) for O and H_2O are 414 and 1329, respectively, which are 200–1000 times larger than those of (a) and makes (b) the dominant part in the 3D turbulent case. Essentially, (a) means the reaction rates of the globally reduced pathways are linearly removed. In contrast, (b) means that the difference in reaction rate coefficients (e.g. activation energy) can be nonlinearly (e.g. exponentially) enlarged. In summary, (b) is the dominant source of the discrepancies between the results using the two models, and it is more sensitive to unsteadiness and other turbulence effects.

Figure 7 shows a comparison of 2D contours of temperature as computed using GRI-Mech 3.0 and the 11-species model. The stoichiometric mixture fraction iso-lines are marked as black curves. Local extinction and re-ignition are clearly captured by both models. At 20 t_j, the extinction level is high (93% of the computational domain is below 1300 K), and only a few discrete flame pockets survive. At 40 t_j, most regions in the shear layers have been re-ignited and the flames are connected. In addition, the shear layers at 40 t_j are spread much more widely than at 20 t_j. The peak combustion intensities (quantified by peak temperature), as modeled using GRI-Mech 3.0 (1627 K at 20 t_j, and 1882 K at 40 t_j), are higher than those from the 11-species model (1547 K at 20 t_j, and 1812 K at 40 t_j); this is consistent with the previously-discussed statistics of T conditioned on Z_{st}. Flame surface area varies by up to 26% (at 20 t_j) between the two chemical kinetics models, and the spatial distribution of combustion intensity is different, especially at 40 t_j. These differences are not revealed by comparison of T versus Z_{st}, because those analyses average out the differences in the spatial distribution of the shear layers and mixture fraction. For this reason, the average of the local point-wise deviation between the two chemical kinetics models is significantly larger than those shown in Table 4. These differences are particularly important in practice, as they can quickly affect the interplay of molecular diffusion, finite-rate kinetics, and turbulent mixing, thus altering the combustion dynamics.

4.4.2. Conditional statistics

The mixture-fraction conditioned mean values of temperature, and mass fractions of OH, O, and H at local extinction (20 t_j) and re-ignition (40 t_j), are shown in Fig. 8. The initial values and the laminar flamelet data at extinction from both chemical kinetics models are obtained by gradually increasing the bulk strain rate in the laminar flamelet calculation until extinction occurs. As shown in Fig. 8, for both chemical kinetics models, the temperature and mass fractions of OH and H decrease below the extinction values of the laminar flamelet solution at 20 t_j, indicating approach toward local extinction. Temperatures drop to ~1300 K, which is ~300 K lower than the initial temperatures, and rise again beyond the extinction values at 40 t_j, indicating re-ignition. The behavior of H is different from those of the other three quantities, as it increases continuously regardless of extinction and re-ignition. This is because most H_2 is converted into H and OH radicals within the fuel stream, rather than reacting at the stoichiometric flame

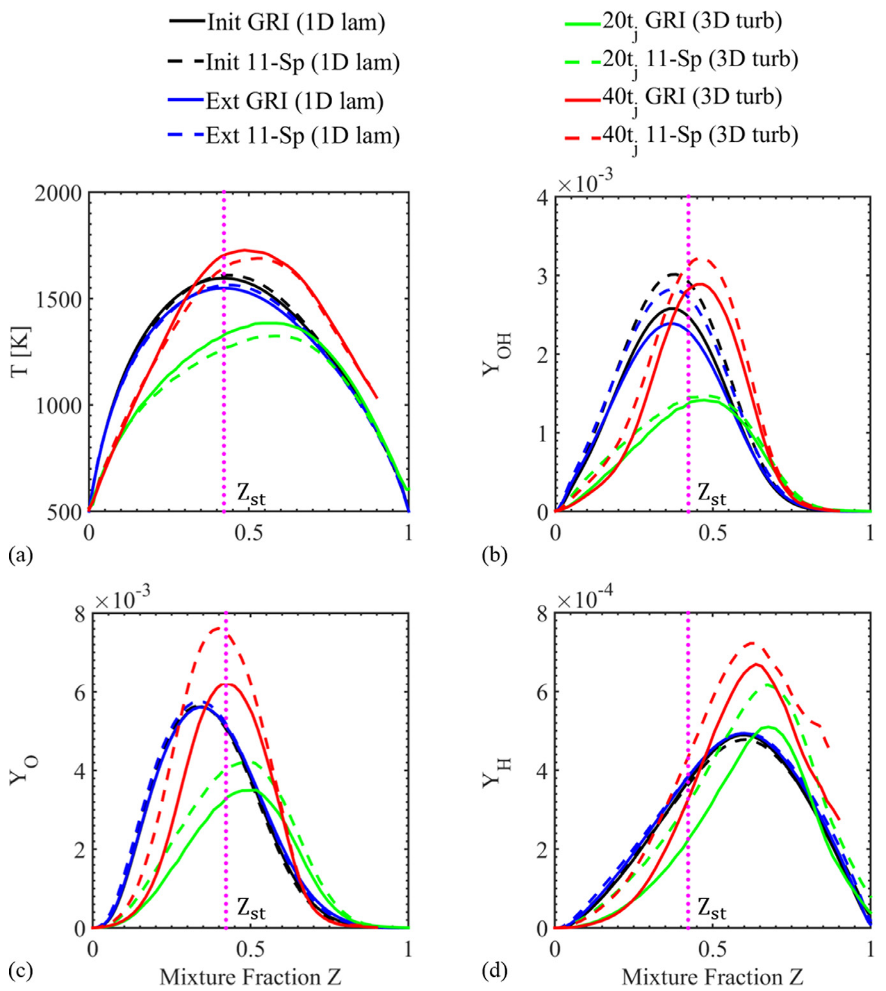

Fig. 8. Comparison of GRI-Mech 3.0 (solid line) and 11-species model (dashed line) in 1D steady laminar solutions (initial data and laminar flamelet values at extinction) and 3D turbulent simulations (at $20t_j$ and $40t_j$): the conditional means of (a) T, (b) Y_{OH}, (c) Y_{O}, and (d) Y_{H}.

surface, and thus it is less affected by the change in the intensity of combustion. The comparison of heat release rates from the two models are shown in Fig. S4 of the Supplementary material. GRI-Mech 3.0 has a higher peak heat release rate than the 11-species model, which explains the higher temperature in the simulation using GRI-Mech 3.0.

Although the predictions from the two chemical kinetics models show the same trends, the 11-species model predicts lower temperature and higher radical levels at all mixture fractions. In other words, it predicts a lower radicals-to-products conversion rate for heat release. As a result, the 11-species model predicts more local extinction (mean $T|Z_{st}$ is 49 K smaller) but less reignition (mean $T|Z_{st}$ is 42 K smaller). The largest deviations and peak values of temperature, OH, and O in the 1D steady laminar case are located near the stoichiometric mixture fraction of 0.42. The mixture fractions corresponding to the largest deviations or peak values in 3D turbulent simulations, on the other hand, are all on rich side ($Z > 0.42$), due to the relatively high diffusivities of fuels. For example, at $20\,t_j$, H peaks and deviates most at approximately $Z = 0.7$, a highly rich value. Moreover, all deviations in the 3D turbulent simulations are significantly larger than those in the 1D steady laminar solutions, except for the OH mass fraction, which has different laminar flamelet predictions in the two chemical kinetics models. In contrast, there are no observable errors in the same comparison between the results from the benchmark and from DAC+CoTran (not shown here); this demonstrates that DAC+CoTran technique does not affect the observations presented here. There are only minor deviations between GRI-Mech 3.0 and GRIred11 in the same comparison (not shown here).

The conditional means of mass fractions of CO, H_2, CO_2, and H_2O with respect to mixture fraction from both chemical kinetics models are compared in Fig. 9. Profiles of the conditional Y_{CO} are close to linear, while those of $Y_{\mathrm{H_2}}$ contain significant variations of slope with respect to mixture fraction. More precisely, the slopes of $Y_{\mathrm{H_2}}$ are larger than those of Y_{CO} near $Z=1$ (the fuel stream) because the early consumption of H_2 inside the fuel stream provides H and OH radicals for the oxidation of CO. On the other hand, the slopes of $Y_{\mathrm{H_2}}$ are smaller than those of Y_{CO} near $Z=0$ (the oxidizer stream), due to the recombination of radicals to reform H_2. Following the consumption of fuel, at approximately $Z=0.9$ at $40\,t_j$, the profiles of both Y_{CO} and $Y_{\mathrm{H_2}}$ end.

The behavior of $Y_{\mathrm{CO_2}}$ is similar to that of the OH and O radicals – it is lower than the extinction values at $20\,t_j$ but higher at $40\,t_j$. In contrast, instead of recovering to values exceeding the extinction cutoff, H_2O levels further decrease at $40\,t_j$. There are two reasons for this phenomenon. On one hand, as shown in Fig. 9(a and b), the initial jet contains only 10% H_2 but 50% CO (by volume) so that at $40\,t_j$ there is limited H_2 left in the fuel stream to generate H, OH and H_2O, but a significant amount of CO left for CO_2 generation. On the other hand, thermal decomposition of H_2O ($H_2O+M=H+OH+M$, $H_2O+O=2OH$) dominates the reactions at the

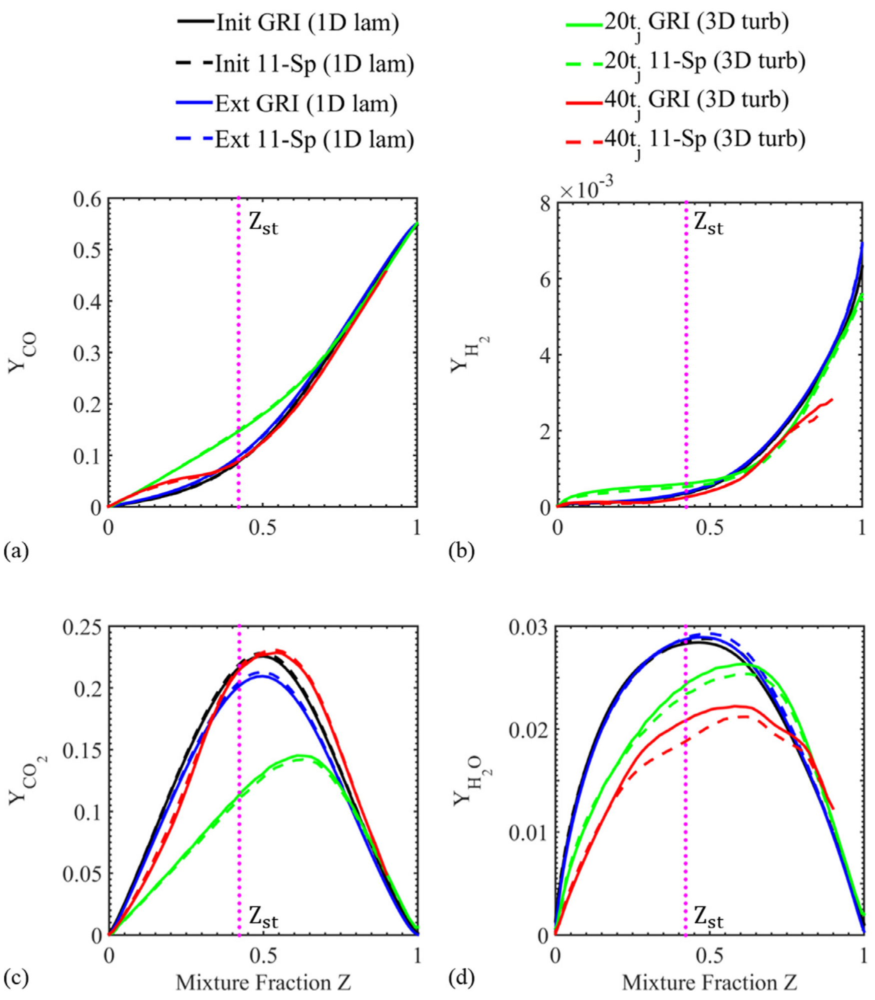

Fig. 9. Mass fractions of (a) CO, (b) H_2, (c) CO_2, and (d) H_2O, in 1D steady laminar solution (initial data and laminar flamelet values at extinction) and 3D turbulent simulations (at $20t_j$ and $40t_j$); GRI-Mech 3.0 (solid line) and 11-species model (dashed line).

high re-ignition temperature, as can be seen in the high level of H and OH at $40\,t_j$, as shown in Fig. 8(b, d).

At $20\,t_j$, as compared with H radical, both products peak and deviate most at above $Z=0.6$, a less-rich value, because of the smaller diffusivities. All predictions of the conditional Y_{CO} from the two chemical kinetics models match well, while there are slight deviations in Y_{H_2} and Y_{CO_2}. Moreover, the 11-species model predicts a significantly lower level of Y_{H_2O} in turbulent simulations (especially in the range of $0.2 < Z < 0.8$), but a slightly higher level in 1D steady laminar solutions. The reason for these opposite deviation trends is that the deviations in H_2O from (a) global reduction in kinetics pathways, and (b) different reaction rate coefficients, are in the opposite direction. Furthermore, (a) dominates the total deviations in 1D steady laminar flames, while (b) dominates in 3D turbulent flames, as discussed in Section 4.4.1. For this reason, for H_2O in 1D steady laminar flames, the deviation between GRI-Mech 3.0 and GRIred11 (contribution from (a): $dev_{abs,\ st}^{H_2O,\ (GRI\ vs\ GRIred11)}$) is larger than the deviation between GRI-Mech 3.0 and the 11-species model (total deviation: $dev_{abs,\ st}^{H_2O,\ (GRI\ vs\ 11-sp)}$). As a result, (a) contributes more than 100% of the total deviation of H_2O in 1D steady laminar flames, as shown in Table 5. Even though, both the total deviation and the contribution from (a) are actually very small (within 0.5%) in 1D steady laminar flames. According to the Arrhenius law, the reaction rate is $\mathrm{RR} = k(T)\prod_k [Y_k]^{\nu'_k}$, and the reaction rate constant is $k(T) = A\,T^b \exp(-\frac{E_a}{RT})$.

In 1D steady laminar solutions, the deviations in species concentration and temperature between the two chemical kinetics models (GRI-Mech 3.0 and the 11-species model) are negligible, so the additional reaction pathways in GRI-Mech 3.0 and the deviations of pre-exponential factor A dominate the total deviations. More precisely, both chemical kinetics models have exactly the same coefficients ($A,\ b, E_a$) for the major H_2O formation reaction (H_2 +OH=H_2O+H), but the pre-exponential factor A of the major decomposition reaction of H_2O (the inverse of H+OH+M=H_2O+M) for GRI-Mech 3.0 is 72% higher than in the 11-species model. This is why the 11-species model predicts a slightly higher level of H_2O and a slightly lower level of H in the 1D steady laminar solution.

In unsteady simulations, on the other hand, the deviations in species concentration and temperature are significantly higher. In addition, according to Table 5 and a comparison of the same conditional statistics between GRI-Mech 3.0 and GRIred11 (not shown here), (a) is not the main driver for these large deviations. This suggests that, instead of deviations in pre-exponential factor A or deviations from (a), deviations in reactant concentration and the nonlinear temperature-dependent term $T^b \exp(-\frac{E_a}{RT})$ are responsible for the total deviations. Note that the 11-species model predicts a lower H_2 level and significantly lower temperature than GRI-Mech 3.0, so that the major H_2O formation pathway (H_2 +OH=H_2O+H) is significantly slower. In addition, this reaction (with $E_a = 3430$ cal/mole) is more sensitive to temperature than H_2O's major decomposition pathway (the inverse of

Table 6
Maximal (over mixture fraction Z) deviations/errors of the conditional means in the 11-species model (11-sp), GRI-Mech 3.0 using DAC+CoTran, and GRIred11, with respect to GRI-Mech 3.0: temperature and mass fractions of representative species.

Absolute deviation	T (K)	Y_{CO}	Y_{H_2}	Y_{O_2}	Y_H	Y_O	Y_{OH}	Y_{CO_2}	Y_{H_2O}
Init. (1D steady laminar): 11-sp	23.28	0.002	0.00003	0.0013	0.00002	0.0002	0.00044	0.003	0.0006
Ext. (1D steady laminar): 11-sp	22.14	0.002	0.00006	0.0017	0.00002	0.0003	0.00044	0.003	0.0006
$20t_j$ (3D unsteady laminar): 11-sp	96.76	0.006	0.00003	0.0062	0.00006	0.0013	0.00057	0.006	0.0023
$40t_j$ (3D unsteady laminar): 11-sp	89.25	0.004	0.00006	0.0027	0.00004	0.0011	0.00060	0.006	0.0019
$20t_j$ (3D turbulent): 11-sp	70.97	0.004	0.00035	0.0085	0.00011	0.0007	0.00017	0.009	0.0022
$40t_j$ (3D turbulent): 11-sp	86.20	0.024	0.00039	0.0056	0.00019	0.0016	0.00057	0.016	0.0023
$20t_j$ (3D turbulent): DAC+CoTran	06.81	0.002	0.00009	0.0005	5.62E−6	5.6E−5	0.00002	0.001	0.0002
$40t_j$ (3D turbulent): DAC+CoTran	11.27	0.004	0.00008	0.0013	0.00002	9.7E−5	0.00004	0.003	0.0004
Init. (1D steady laminar): GRIred11	08.55	0.001	0.00005	0.0002	4.22E−6	4.5E−5	0.00002	0.001	0.0002
$20t_j$ (Turbulent): GRIred11	22.52	0.003	0.00019	0.0015	0.00001	0.0001	0.00006	0.004	0.0007
$40t_j$ (Turbulent): GRIred11	14.39	0.002	0.00006	0.0015	0.00002	9.9E−5	0.00005	0.002	0.0002
Rel. deviation (%)	T	Y_{CO}	Y_{H_2}	Y_{O_2}	Y_H	Y_O	Y_{OH}	Y_{CO_2}	Y_{H_2O}
Init. (1D steady laminar): 11-sp	1.52	01.36	31.18	4.11	30.69	08.89	17.61	01.16	02.47
Ext. (1D steady laminar): 11-sp	1.49	01.36	00.89	4.54	16.29	10.71	18.50	01.49	02.37
$20t_j$ (3D unsteady laminar): 11-sp	5.08	05.47	06.52	3.05	34.07	47.08	28.55	02.59	07.66
$40t_j$ (3D unsteady laminar): 11-sp	4.59	10.62	03.09	2.77	47.64	54.13	29.72	02.85	06.64
$20t_j$ (3D turbulent): 11-sp	5.26	73.41	07.79	2.95	23.64	21.46	32.49	30.80	62.36
$40t_j$ (3D turbulent): 11-sp	5.46	05.21	14.51	5.56	58.99	33.51	26.05	14.56	11.16
$20t_j$ (3D turbulent): DAC+CoTran	1.02	00.35	02.28	0.002	01.15	01.60	01.44	04.23	04.57
$40t_j$ (3D turbulent): DAC+CoTran	1.00	01.00	02.98	0.011	05.44	02.34	03.53	06.30	02.40
Init. (1D steady laminar): GRIred11	0.99	00.20	01.23	00.78	02.16	00.83	00.76	02.80	0.57
$20t_j$ (Turbulent): GRIred11	3.68	00.50	03.26	00.48	03.22	04.52	04.68	04.76	03.86
$40t_j$ (Turbulent): GRIred11	1.00	00.38	02.25	01.11	06.99	01.60	02.63	01.78	01.12

H+OH+M=H_2O+M with $E_a = 0$), so that the H_2O decomposition rates in the two chemical kinetics models are similar. These considerations explain why the 11-species model predicts a significantly lower H_2O level in unsteady simulations. In summary, the deviations in species concentration, temperature, and reaction rates form a nonlinear positive feedback loop in unsteady simulations, which significantly magnifies the sensitivity of simulation results to chemical kinetics models.

To provide further quantitative detail on the conditional mean deviations between the two chemical kinetics models, absolute and relative deviations of the 1D steady laminar flame (initial and at extinction), 3D unsteady laminar flame (both $20\,t_j$ and $40\,t_j$), and turbulent flame (both $20\,t_j$ and $40\,t_j$) using the two chemical kinetics models are presented in Table 6. The absolute conditional mean deviation of an arbitrary quantity ϕ is defined as:

$$dev^{\phi}_{abs} = \max_{0 \le Z \le 1} \left| \langle \phi_{GRI} | Z \rangle - \langle \phi_{11-sp} | Z \rangle \right| \tag{6}$$

and its relative conditional mean deviation is defined as:

$$dev^{\phi}_{rel} = \max_{0 \le Z \le 1} \left| \frac{\langle \phi_{GRI} | Z \rangle - \langle \phi_{11-sp} | Z \rangle}{\langle \phi_{GRI} | Z \rangle} \right| \tag{7}$$

For the 1D steady laminar case in Table 6, approximately 31% relative deviation of H and H_2 happens near $Z=1$ (pure fuel) and $Z=0$ (pure oxidizer), where the concentrations of H and H_2 are close to zero (see Figs. 8 and 9) resulting in large deviation. Similar to the trend shown in Table 4, the deviations in Table 6 increase sharply from the 1D steady laminar to the 3D unsteady laminar to the 3D turbulent for most quantities, including temperature and major species. As shown in Table 4, the relative deviation in 3D turbulent simulations can be more than 50 times larger than that in the 1D steady laminar solutions for CO, almost 20 times for H_2, almost 30 times larger for CO_2 and H_2O, and nearly 4 times larger for temperature. The absolute deviation magnification factor is 4 for temperature, 12 for CO, 13 for H_2, 7 for O_2, 5 for CO_2, and 4 for H_2O. This further proves that the effects of unsteadiness and turbulence can significantly increase the deviations between the two chemical kinetics models, not only on the stoichiometric surface, but also for all values of mixture fraction. Again, the effect of unsteadiness is larger than that of turbulence for most quantities, because the major influence of turbulence is on the spatial distribution of the shear layer flow field and mixture fraction, and the spatial distribution is diminished in both Tables 4 and 6. Therefore, the observed deviation magnification in the turbulent case is not primarily due to the chaotic system and strange attractor. Compared to the unsteady laminar case, the addition of turbulence amplifies the deviations for some quantities, but reduces the deviations for some others. The former ones may come from different attractors in the chaotic system. However, for the latter ones, either chaos is not the dominant factor, or the altered attractor is very close to the original attractor in the chaotic system. At $20\,t_j$, the deviation in unsteady simulation is nearly 100 K, which is hardly acceptable for high-fidelity prediction, and could significantly affect the prediction of many important quantities, including NO_x emission.

To verify that DAC+CoTran does not affect the above observations, Table 6 also provides its error quantification using Eqs. (6) and (7). The errors are one half to three orders of magnitude smaller than the corresponding differences between the two chemical kinetics models. Table 6 also includes the differences between GRI-Mech 3.0 and GRIred11 to show the contribution from the global reduction of kinetics pathways to the total deviations.

To better understand the contribution to the total deviations from (a) the global reduction of kinetics pathways, and from (b) the differences in reaction rate coefficients, Table 7 shows the contribution of (a) to the total absolute deviations between the two chemical kinetics models, and the absolute deviation magnification factors for (a), (b), and total. The contribution of (a) is defined as the ratio of the deviations between GRI-Mech 3.0 and GRIred11 to the deviations between GRI-Mech 3.0 and the 11-species model: $C^{\phi}_{(a)} = dev^{\phi,\ (GRI\ vs\ GRIred11)}_{abs} / dev^{\phi,\ (GRI\ vs\ 11-sp)}_{abs}$. In the 1D steady laminar case, part (b) dominates the total deviations for most quantities except fuels (CO and H_2). In the 3D turbulent case, part (b) dominates the total deviations for all quantities. Both (a) and (b) are sensitive to unsteadiness and other turbulence effects, but for temperature and all major species, (b) is more sensitive than (a). In particular, (a) contributes approximately 50% of the deviation for CO and more than 100% for H_2 in the 1D steady laminar case, which indicates that (a) and (b) cause deviations in opposite directions for H_2. However, the magnification factors of (b)

Table 7
Contribution from the global reduction of reaction pathways to the maximal (over mixture fraction Z) absolute deviations between GRI-Mech 3.0 and the 11-species model; absolute deviation magnification factors for (a) global reduction of reaction pathways and (b) different reaction rate coefficients, and total. Temperature and mass fractions of representative species.

Contribution from (a) to total deviation (%)	T	Y_{CO}	Y_{H_2}	Y_{O_2}	Y_H	Y_O	Y_{OH}	Y_{CO_2}	Y_{H_2O}
1D steady laminar	36.73	50.0	>100	15.38	21.10	22.50	04.55	33.33	33.33
3D turbulent	26.13	12.5	48.72	17.65	10.53	06.25	10.53	25.00	30.43
Deviation magnification factor	T	Y_{CO}	Y_{H_2}	Y_{O_2}	Y_H	Y_O	Y_{OH}	Y_{CO_2}	Y_{H_2O}
(a) Reduced kinetics pathways	2.63	03	03.8	7.50	04.74	2.22	3.00	4.00	3.50
(b) Different RR coefficients	4.32	21	10.0	6.36	10.77	9.68	1.21	6.00	4.00
Total	3.89	12	13.0	6.54	09.50	8.00	1.30	5.33	3.83

for O and H_2O are 21 and 18, respectively, which are 6–7 times larger than those of (a) and makes (b) the dominant factor in the 3D turbulent case. In addition, with only (a), even after the large deviation magnification (up to 7.5 times), the deviations are still within ~2% for temperature and major species. The global mechanism reduction can thus still be considered appropriate for use. In summary, (b) dominates the deviations and is more sensitive to unsteadiness and other turbulence effects.

We note that the above observations were shown to be insensitive to grid resolution in the grid convergence test, as presented in Fig. S1 of the Supplementary material. When the grid resolution is increased by a factor of 2 in all spatial directions, the temperature and mass fractions of H_2O and H only change up to approximately 0.5% (7 K), 1%, and 5%, respectively. In contrast, for both grid resolutions, the deviations between the two chemical kinetics models in temperature and mass fractions of H_2O and H are approximately 6% (84 K), 6%, and 20%, respectively, and these sizes are independent of the grid refinement. The spatially averaged transverse profiles provide similar mesh-independent results. When the grid resolution is increased by a factor of 2 in all spatial directions, the temperature and mass fractions of H_2O and H only change up to approximately 1% (10 K), 1%, and 6.5%, respectively. In contrast, for both grid resolutions, the deviations between the two chemical kinetics models in temperature and mass fractions of H_2O and H are approximately 5.3% (67 K), 5.5%, and 40%, respectively, and these sizes are independent of the grid refinement.

4.4.3. Syngas flame structure

To further investigate the effects of turbulence, which are not clear from the statistics in mixture fraction space, 2D contours of vorticity magnitude and mixture fraction obtained from turbulent simulations are shown in Figs. 10 and 11, respectively. The two chemical kinetics models produce similar vorticity magnitude and mixture fraction fields at $20\,t_j$ (local extinction), but significantly different fields at $40\,t_j$ (re-ignition). However, the same comparison for 3D unsteady laminar simulations (not shown here) shows almost identical vorticity magnitude and mixture fraction fields from both the chemical kinetics models, with less than 0.6% deviations in peak values. The deviations in flow and mixture fraction field seem therefore likely to be the result of the complex turbulence–chemistry interaction. Furthermore, the vorticity magnitude field does not contain the initial isotropic turbulence at

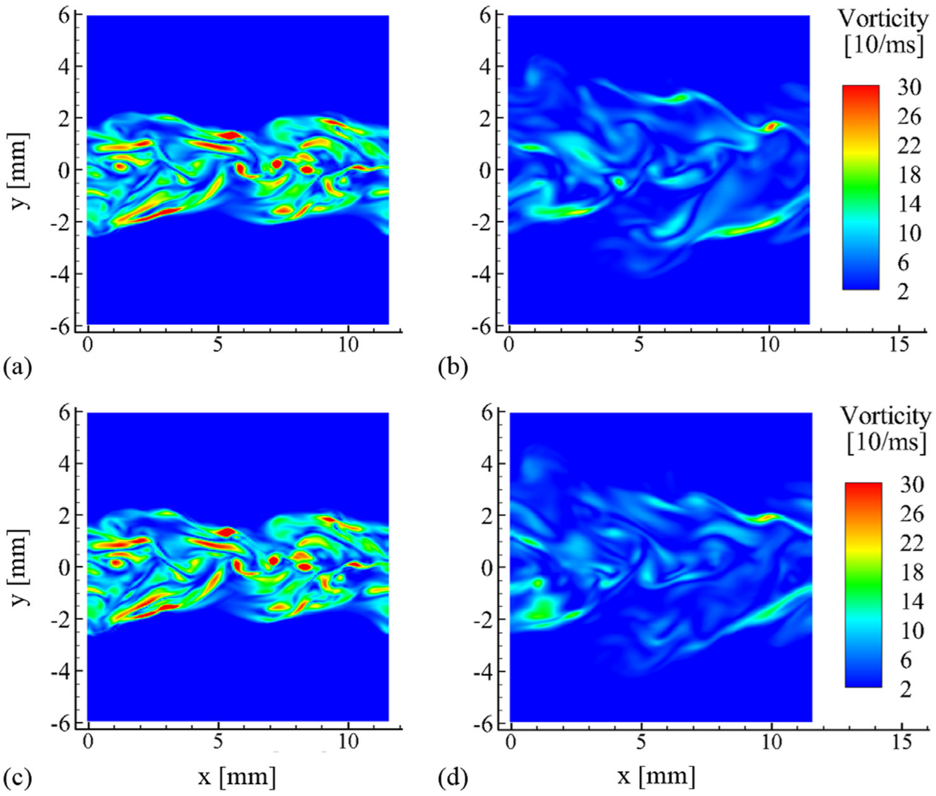

Fig. 10. Comparison of GRI-Mech 3.0 (upper) and 11-species model (lower): instantaneous 2D contours of vorticity magnitude at $20\,t_j$ (left) and $40\,t_j$ (right) on center plane ($Z = 4H$).

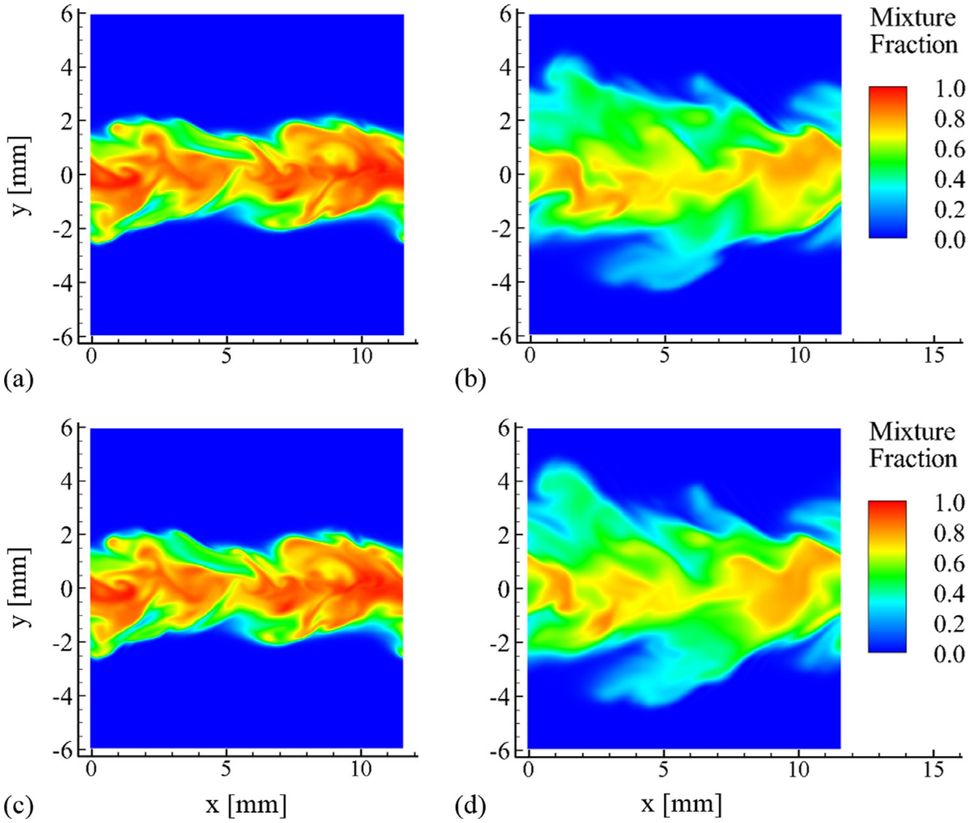

Fig. 11. Comparison of GRI-Mech 3.0 (upper) and 11-species model (lower): instantaneous 2D contours of mixture fraction at $20\,t_j$ (left) and $40\,t_j$ (right) on center plane ($Z=4$H).

both time instants, but is dominated by the shear-generated turbulence triggered by the initial turbulence. At both time instants, the stoichiometric mixture fraction value of 0.42 is found inside the shear layers.

The 2D contours of Y_{CO} and Y_{H_2} in turbulent simulations using the two chemical kinetics models are shown in Figs. 12 and 13, respectively. Due to fuel consumption, the levels of both CO and H_2 decrease significantly from $20\,t_j$ to $40\,t_j$. As shown in Fig. 9, the consumption of H_2 is much faster than that of CO, as is consistent with the conditional statistics. This is because CO can only be consumed by combustion near the stoichiometric surface, but H_2 can be consumed inside the hot fuel stream by thermal decomposition (chain initiation reaction H_2 +M=2H+M); this effect is also suggested by the spatial distribution of consumption rates of CO and H_2 (not shown here). In Fig. 9, at $20\,t_j$, the major deviations between the two chemical kinetics models are in the peak values and the volume occupied by the peak values, as is further demonstrated by the conditional mean statistics. In contrast, the deviations at $40\,t_j$ are primarily in the spatial distribution, which is controlled by the flow field deviations shown in Fig. 10.

Since OH is the key radical consuming CO and releasing heat, its 2D contours from the two chemical kinetics models are presented in Fig. 14. Interestingly, the contours of OH roughly wrap around those of H_2 in Fig. 13, which means that OH is mainly generated from the remaining H_2 in the fuel stream via chain branching reactions (i.e., H+O_2 =O+OH, O+H_2 =H+OH). The behavior of OH is similar to that of temperature in Fig. 7, which indicates local extinction and re-ignition. Even at $20\,t_j$, however, a few disconnected small OH pockets survive and become the source of later re-ignition. A larger spread of OH in the transverse direction is clearly observed in the 11-species model as compared to GRI-Mech 3.0, especially at $40\,t_j$; this also demonstrates that the model with a lower radicals-to-products conversion rate (11-species model) can cause more local extinction and less re-ignition under the effect of turbulence.

4.4.4. Scalar dissipation rate statistics

Figure 15 presents a comparison of the two chemical kinetics models through 2D contours in the symmetry plane of the scalar dissipation rate $\chi = 2D\nabla Z \cdot \nabla Z$, normalized by its extinction value $\chi_q = 961\ \text{sec}^{-1}$, where D is the mixture diffusivity, assuming unity Lewis numbers. A logarithmic scale is used here to account for the wide range of the scalar dissipation rate field. The stoichiometric mixture fraction iso-lines are marked as black curves. The contours clearly show that the flow is fully turbulent, and the high dissipation regions are concentrated in thin “laminar” sheets. The scalar dissipation rate is much more spatially distributed at $40\,t_j$ than at $20\,t_j$, due to more transverse spreading of the shear layers, but the peak values are similar. The thin sheets of peak values are generally located near the stoichiometric surface, where mixture fraction has the largest gradients. As in the flow and mixture fraction fields, the two chemical kinetics models produce similar scalar dissipation rate distributions at $20\,t_j$ (local extinction) and different at $40\,t_j$ (re-ignition), but the two chemical kinetics models show almost identical scalar dissipation rate fields in the 3D unsteady laminar simulations (not shown here). This suggests that the deviations in scalar dissipation rate also come from the turbulence–chemistry interaction.

In order to remove possible bias resulting from the unmixed oxidizer fluid [46], Fig. 16 shows a comparison of the normalized PDFs of scalar dissipation rate on the stoichiometric surface (Z_{st}) from both chemical kinetics models. Results from the two chemical kinetics models match well, except for some slight deviations in

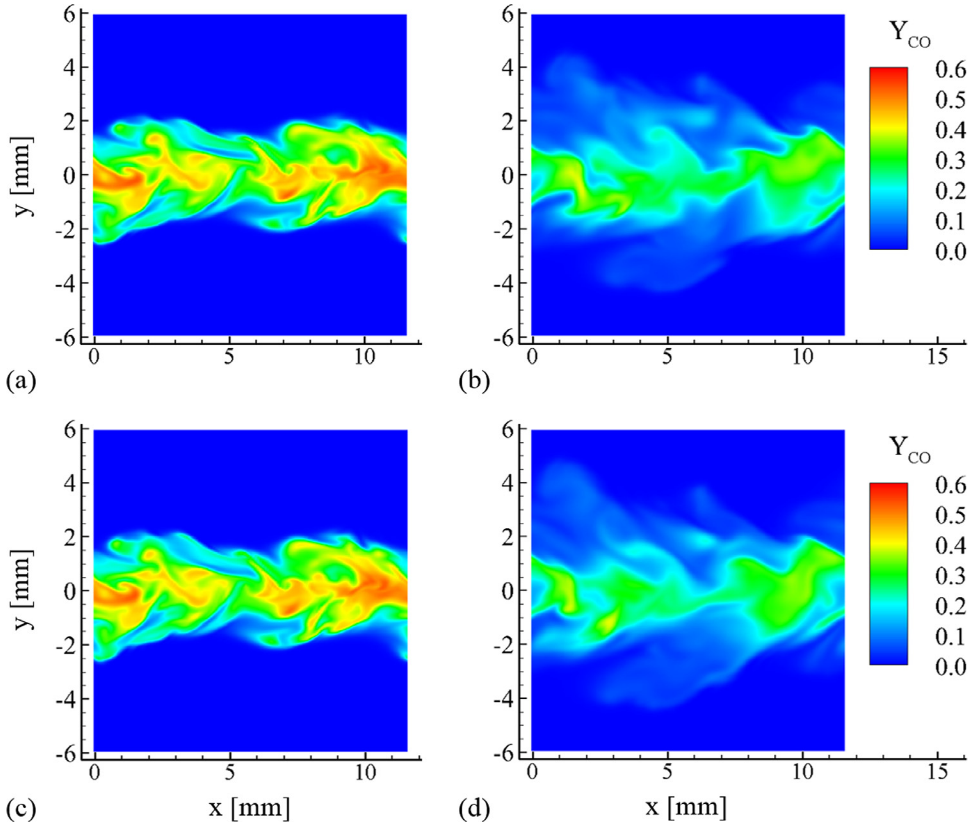

Fig. 12. Instantaneous 2D contours of CO mass fraction at 20 t_j (left) and 40 t_j (right) on the center plane (Z=4H): GRI-Mech 3.0 (upper) and 11-species model (lower).

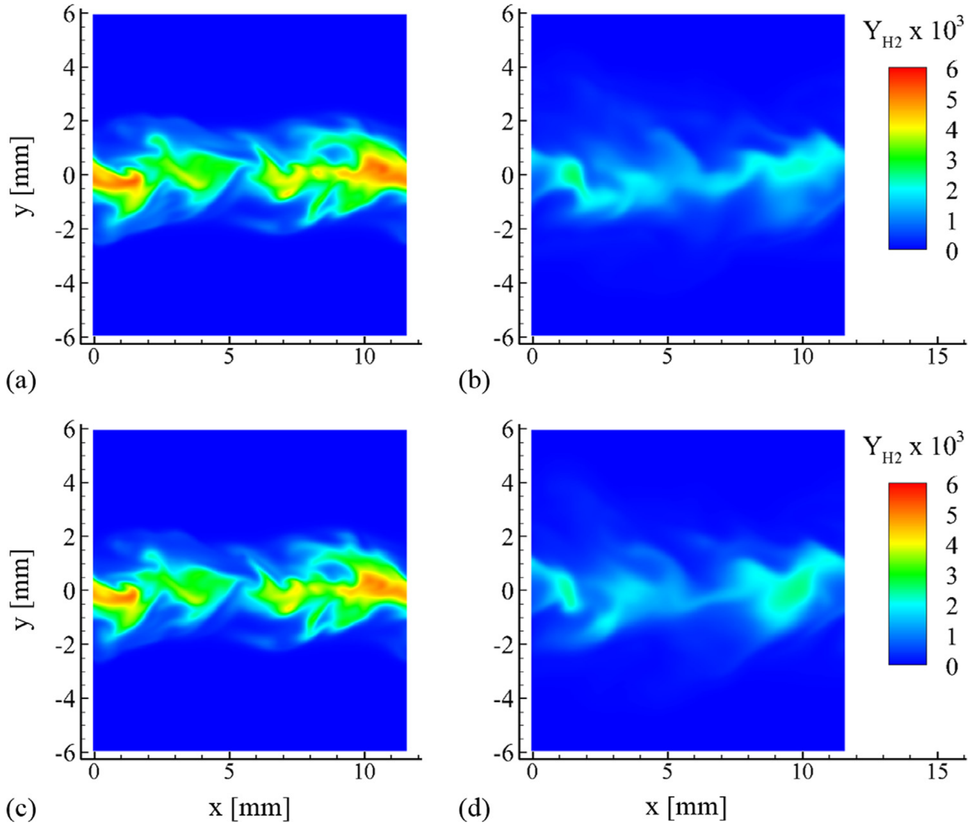

Fig. 13. Instantaneous 2D contours of H_2 mass fraction at 20 t_j (left) and 40 t_j (right) on the center plane (Z=4H): GRI-Mech 3.0 (upper) and 11-species model (lower).

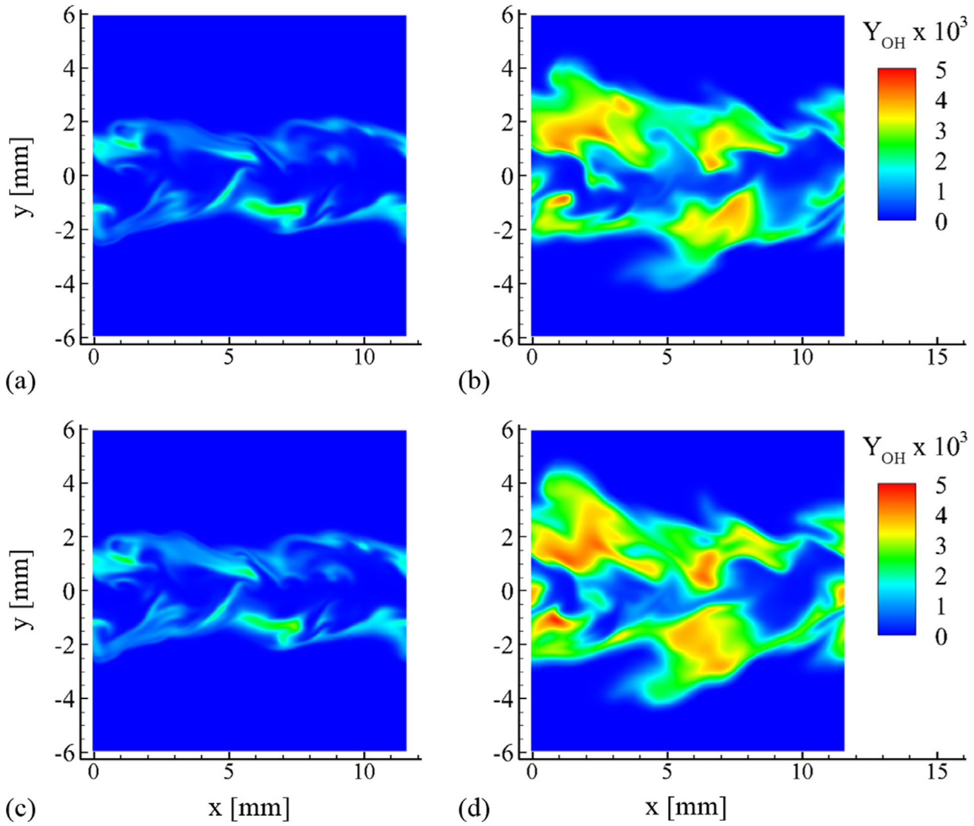

Fig. 14. Instantaneous 2D contours of OH mass fraction at 20 t_j (left) and 40 t_j (right) on the center plane (Z=4H): GRI-Mech 3.0 (upper) and 11-species model (lower).

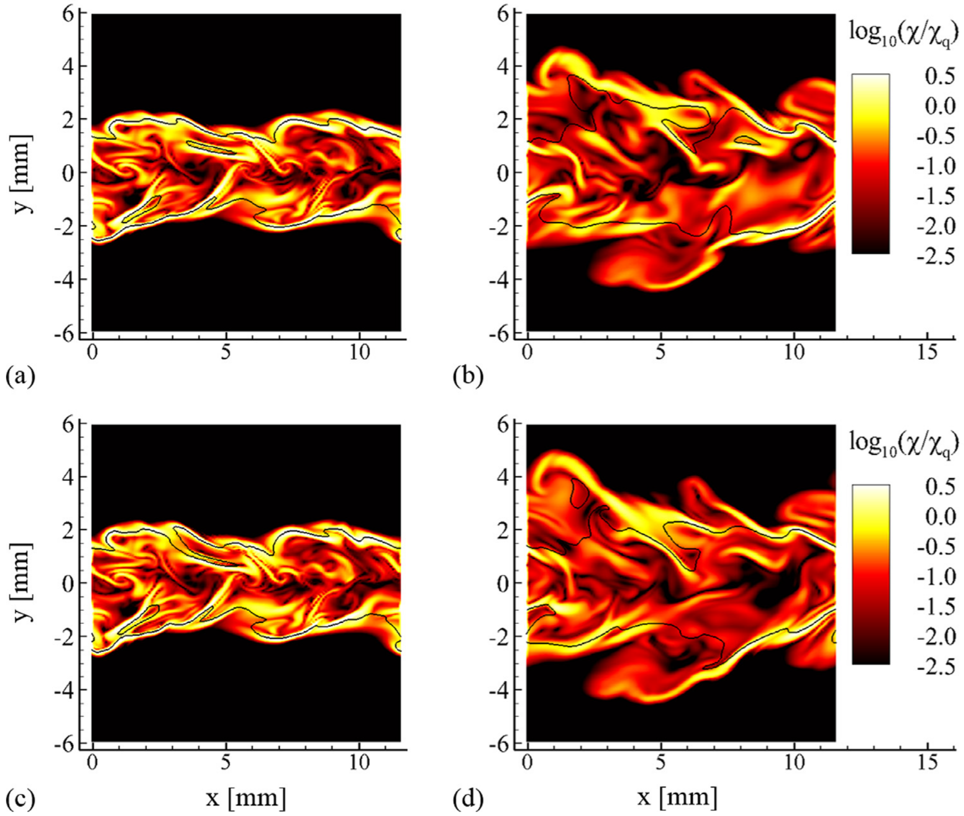

Fig. 15. Instantaneous 2D contours of $\log_{10}(\chi/\chi_q)$ at 20 t_j (left) and 40 t_j (right) on the center plane (Z=4H): GRI-Mech 3.0 (upper) and 11-species model (lower).

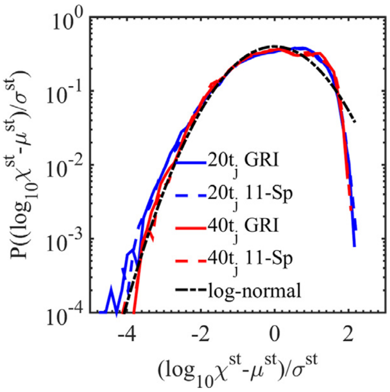

Fig. 16. PDF of normalized logarithm of scalar dissipation rate on the stoichiometric surface at $20\,t_j$ (blue) and $40\,t_j$ (red): GRI-Mech 3.0 (solid lines), 11-species model (dashed lines), and log–normal distribution (dash-lot line). (For interpretation of the references to color in this figure legend, the reader is referred to the web version of this article.)

the left tail (normalized $\chi_{st} < -3$). The results from both chemical kinetics models match well even for the un-normalized PDF, with the detailed comparison shown in Table 8. Re-ignition ($40\,t_j$) has a slightly smaller mean scalar dissipation rate than local extinction ($20\,t_j$), due to the spreading of mixture fraction.

Both chemical kinetics models show a negatively skewed mono-modal log–normal-like distribution with small departure from the ideal log–normal distribution on both tails [46]. With respect to the ideal log–normal distribution, they both over-predict the PDF at the left tail (normalized $\chi_{st} < -2$) and under-predict the PDF at the right tail (normalized $\chi_{st} > 2$). This is the so-called "scalar intermittency" in turbulent mixing theory [13]. Therefore, the log–normal distribution, which is applied in flamelet methods to model χ_{st} [47], has low accuracy at high and low values of χ_{st}, but good accuracy for the rest region. Interestingly, re-ignition ($40\,t_j$) is slightly closer to the log–normal distribution than local extinction ($20\,t_j$), which indicates that the amount of intermittency decreases with the temporal evolution. Thus, the log–normal model in flamelet methods may perform better in long-term simulations of time-evolving problems, in which turbulence decays. The log–normal-like distribution is consistent with the results from the DNS study with over-resolved grid of Hawkes et al. [13] (this further confirms the use of reasonable grids in the present study). As tested, the continuous log–normal-like distribution of χ_{st} is only seen in turbulent combustion, while both 1D steady and 3D unsteady laminar simulations contain only one single value of χ_{st} .

The standard scalar dissipation rate χ is defined based on mixture fraction. At the same time, each species has its own scalar dissipation rate, defined as $\chi_k = 2D_k \nabla Y_k \cdot \nabla Y_k$ for the kth species, where D_k is its mass diffusivity. As in Fig. 16, normalized PDFs of stoichiometric χ_{CO} and χ_{OH} in the turbulent cases also approximately follow the log–normal distribution, except in the two tails, while laminar cases only contain a few discrete values of stoichiometric χ_{CO} and χ_{OH} (not shown here). Figure 17 presents the PDF of χ/χ_q, χ_{CO}, and χ_{OH} on the stoichiometric surface. The stoichiometric PDFs of χ and χ_{CO} are similar to that of temperature (Fig. 6), but are different from that of χ_{OH} (which is more closely normally distributed). The most likely χ_{st} of local extinction ($20\,t_j$) is 3.5 times larger than χ_q from the flamelet solution, while that of re-ignition ($40\,t_j$) is almost 2 times smaller than χ_q. This result is consistent with the theory that short local time-scales could prevent chemical reactions from releasing enough heat to sustain combustion, and would thus result in extinction [48]. On the other hand, re-ignition ($40\,t_j$) has narrower PDFs than local extinction ($20\,t_j$) for all three scalar dissipation rates, for the same reason as

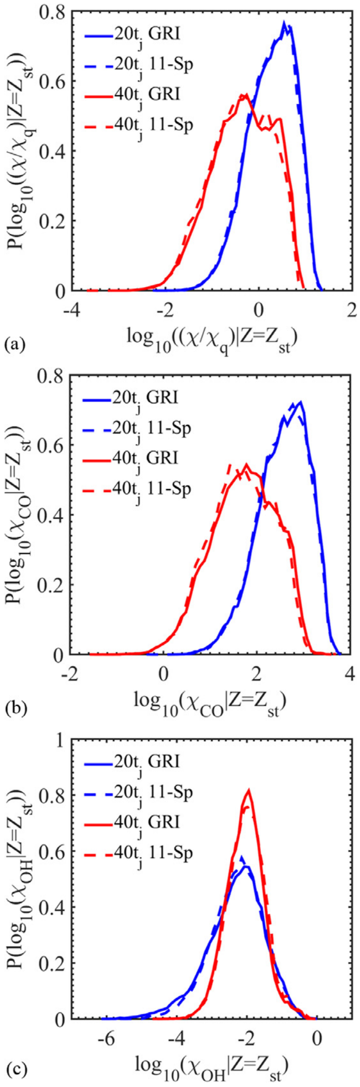

Fig. 17. PDF of (a) χ/χ_q, (b) χ_{CO}, and (c) χ_{OH} on the stoichiometric surface at $20\,t_j$ (blue) and $40\,t_j$ (red), calculated using GRI-Mech 3.0 (solid lines) and 11-species model (dashed lines). (For interpretation of the references to color in this figure legend, the reader is referred to the web version of this article.)

Table 8
Statistics of non-normalized PDFs of scalar dissipation rate on stoichiometric surface (Z_{st}) from the two chemical kinetics models.

Statistics	GRI-Mech 3.0 ($20\,t_j$)	11-species model ($20\,t_j$)	GRI-Mech 3.0 ($40\,t_j$)	11-species model ($40\,t_j$)
Mean	3.25	3.23	2.64	2.59
2nd central moment	0.25	0.25	0.43	0.42
Standard deviation	0.50	0.50	0.66	0.65
3rd central moment	−0.06	−0.06	−0.10	−0.08
Skewness	−0.48	−0.45	−0.34	−0.31

the PDFs of temperature in Fig. 6. For the PDFs of all three scalar dissipation rates, the deviations between the two chemical kinetics models are small near the peak values. For both steady and unsteady laminar simulations, the PDFs of all scalar dissipation rates are mono-modal. Unlike 1D steady laminar simulations, however, the 3D unsteady laminar simulations using the two chemical kinetics models have different principal modes of scalar dissipation rates: only ~2% difference for χ, but 5–6% for χ_{CO}, and 20–55% for χ_{OH}, due to the unsteady shear layer expansion. The high sensitivity to (species-based) scalar dissipation rates results in large deviations in temperature and species concentrations in 3D unsteady laminar simulations.

5. Conclusion

To study the sensitivity of predictions to chemical kinetics models, two chemical kinetics models, GRI-Mech 3.0 [31] and an 11-species syngas model [13], are compared in a 3D finite-rate simulation of a temporally evolving turbulent non-premixed syngas flame with extinction and re-ignition.

Using the ODEPIM solver, techniques of dynamic adaptive chemistry (DAC) and correlated transport (CoTran) are verified and applied, and are found to allow 4 times more efficient computation of 3D finite-rate simulations of turbulent combustion using detailed GRI-Mech 3.0. Comprehensive verifications indicate that DAC+CoTran provides accurate results that allow for comparison of predictions by the two chemical kinetics models.

Local extinction and re-ignition are clearly captured by both chemical kinetics models, with similar qualitative trends. However, significant quantitative deviations are observed, indicating that simulation of turbulent combustion is highly sensitive to the choice of chemical kinetics model. In particular, the temperatures predicted by the 11-species model are consistently lower than those predicted by GRI-Mech 3.0 in stoichiometric PDFs and means (~86 K), conditional statistics (nearly 100 K), and 2D contours. This is due to the presence of fewer radicals-to-products conversions to release heat in the 11-species model. This is also manifested as prediction of more local extinction (mean $T|Z_{st}$ is 49 K smaller) and less re-ignition (mean $T|Z_{st}$ is 42 K smaller). As expected, the mixture-fraction conditioned mean deviations in major species are smaller than those in intermediate and minor species. In the conditional statistics on the major species, the deviations are significant for H_2O, moderate for H_2 and CO_2, and negligible for CO.

Although the two models start with almost identical 1D steady laminar flamelet solutions, the prediction of the 11-species model gradually deviates from that of GRI-Mech 3.0. The deviations in species concentration, temperature, and reaction rates form an interaction cycle to gradually reinforce each other under the effects of unsteadiness and turbulence. This reinforcement can change the dominant factors from the global reduction of kinetics pathways to the deviations in reaction rate coefficients, causing deviations in directions opposite to those seen in 1D steady laminar solutions. In general, the deviations between the two chemical kinetics models increase sharply from the 1D steady laminar to the 3D unsteady laminar to the 3D turbulent simulations for most quantities, including temperature and major species. Thus, the absolute deviation in turbulent combustion simulations is up to 7 times larger than that in the 1D steady laminar solutions for temperature, up to 12 times larger for CO, up to 13 times larger for H_2, up to 7 times larger for O_2, up to 5 times larger for CO_2, and up to 13 times larger for H_2O. We conclude that the effects of unsteadiness and turbulence significantly magnify the sensitivity of turbulent combustion simulation to chemical kinetics. The deviations between the two chemical kinetics models include two major sources: (a) GRI-Mech 3.0 contains 42 more species than the 11-species model, and thus contains 293 more kinetic reactions related to those 42 species; and (b) for those reactions included in both models, the reaction rate coefficients are different. Both (a) and (b) are sensitive to unsteadiness and other turbulence effects, but (b) is the dominant part and is more sensitive to unsteadiness and other turbulence effects. Essentially, (a) means the reaction rates of those globally reduced kinetics pathways, which are linearly removed from the net path fluxes. In contrast, (b) the difference in reaction rate coefficients can grow exponentially.

In the stoichiometric means and conditional statistics of most quantities, the magnification of the deviations between the two chemical kinetics models due to unsteadiness is larger than that due to turbulence. Therefore, the effect of unsteadiness dominates the deviation in mixture fraction space. The two chemical kinetics models provide similar spatial distribution of vorticity magnitude, mixture fraction, and scalar dissipation rates at local extinction, but completely different fields at re-ignition, and these are dominated by the complex turbulence–chemistry interaction.

Both chemical kinetics models show negatively skewed mono-modal log–normal-like distributions for scalar dissipation rates, with small departures on both tails (that is, scalar intermittency). The log–normal distribution, which is used in flamelet methods to model χ_{st}, is not accurate enough at high and low values of χ_{st}, but should have good accuracy for the remaining region. Interestingly, re-ignition is slightly closer to the log–normal distribution than local extinction, which tends to indicate that the amount of intermittency decreases with temporal evolution, so the log–normal model in flamelet methods might perform better for time-evolving problems with decaying turbulence. Due to the expansion of the unsteady shear layer, the two chemical kinetics models have different principal modes of the scalar dissipation rates. Consequently, the high sensitivity to scalar dissipation rates results in large deviations in temperature and species concentrations between the two models.

Acknowledgment

This work was funded partly by NASA (Grant NNX15AU96A), and partly by the William R.T. Oakes Endowment of the Georgia Institute of Technology. The computational resources provided by the DOD HPC at the AFRL centers is greatly appreciated.

Supplementary materials

Supplementary material associated with this article can be found, in the online version, at doi:10.1016/j.combustflame.2017.05.016.

References

[1] H. Pitsch, Large-eddy simulation of turbulent combustion, Annu. Rev. Fluid Mech. 38 (2006) 453–482.
[2] C. Bruno, V. Sankaran, H. Kolla, J.H. Chen, Impact of multi-component diffusion in turbulent combustion using direct numerical simulations, Combust. Flame 162 (11) (2015) 4313–4330.
[3] B. Yenerdag, N. Fukushima, M. Shimura, M. Tanahashi, T. Miyauchi, Turbulence–flame interaction and fractal characteristics of H_2–air premixed flame under pressure rising condition, Proc. Combust. Inst. 35 (2) (2015) 1277–1285.
[4] A. Aspden, M. Day, J. Bell, Lewis number effects in distributed flames, Proc. Combust. Inst. 33 (1) (2011) 1473–1480.
[5] Z. Nikolaou, N. Swaminathan, Direct numerical simulation of complex fuel combustion with detailed chemistry: physical insight and mean reaction rate modeling, Combust. Sci. Technol. 187 (11) (2015) 1759–1789.
[6] A. Aspden, M. Day, J. Bell, Three-dimensional direct numerical simulation of turbulent lean premixed methane combustion with detailed kinetics, Combust. Flame 166 (2016) 266–283.
[7] M. Sheikhi, T. Drozda, P. Givi, F. Jaberi, S. Pope, Large eddy simulation of a turbulent nonpremixed piloted methane jet flame (Sandia Flame D), Proc. Combust. Inst. 30 (1) (2005) 549–556.
[8] M. Ihme, H. Pitsch, Prediction of extinction and reignition in nonpremixed turbulent flames using a flamelet/progress variable model: 2. Application in LES of Sandia flames D and E, Combust. Flame 155 (1) (2008) 90–107.

[9] Y.C. See, M. Ihme, Effects of finite-rate chemistry and detailed transport on the instability of jet diffusion flames, J. Fluid Mech. 745 (2014) 647–681.

[10] X. Wang, V. Yang, Supercritical mixing and combustion of liquid-oxygen/kerosene Bi-swirl injectors, J. Propuls. Power 33 (2) (2017) 316–322.

[11] C. Pantano, Direct simulation of non-premixed flame extinction in a methane–air jet with reduced chemistry, J. Fluid Mech. 514 (2004) 231–270.

[12] E.R. Hawkes, R. Sankaran, J.C. Sutherland, J.H. Chen, Direct numerical simulation of turbulent combustion: fundamental insights towards predictive models, J. Phys.: Conf. Ser. 16 (2005) 65–79.

[13] E.R. Hawkes, R. Sankaran, J.C. Sutherland, J.H. Chen, Scalar mixing in direct numerical simulations of temporally evolving plane jet flames with skeletal CO/H_2 kinetics, Proc. Combust. Inst. 31 (1) (2007) 1633–1640.

[14] B.A. Sen, E.R. Hawkes, S. Menon, Large eddy simulation of extinction and reignition with artificial neural networks based chemical kinetics, Combust. Flame 157 (3) (2010) 566–578.

[15] D.O. Lignell, J.H. Chen, H.A. Schmutz, Effects of Damköhler number on flame extinction and reignition in turbulent non-premixed flames using DNS, Combust. Flame 158 (5) (2011) 949–963.

[16] Y. Yang, H. Wang, S.B. Pope, J.H. Chen, Large-eddy simulation/probability density function modeling of a non-premixed CO/H_2 temporally evolving jet flame, Proc. Combust. Inst. 34 (1) (2013) 1241–1249.

[17] R.W. Bilger, S.B. Pope, K.N.C. Bray, J.F. Driscoll, Paradigms in turbulent combustion research, Proc. Combust. Inst. 30 (1) (2005) 21–42.

[18] T. Lu, C.K. Law, A directed relation graph method for mechanism reduction, Proc. Combust. Inst. 30 (1) (2005) 1333–1341.

[19] P. Pepiot-Desjardins, H. Pitsch, An efficient error-propagation-based reduction method for large chemical kinetic mechanisms, Combust. Flame 154 (1-2) (2008) 67–81.

[20] W. Sun, Z. Chen, X. Gou, Y. Ju, A path flux analysis method for the reduction of detailed chemical kinetic mechanisms, Combust. Flame 157 (7) (2010) 1298–1307.

[21] X. Gao, S. Yang, W. Sun, A global pathway selection algorithm for the reduction of detailed chemical kinetic mechanisms, Combust. Flame 167 (2016) 238–247.

[22] L. Liang, J.G. Stevens, J.T. Farrell, A dynamic adaptive chemistry scheme for reactive flow computations, Proc. Combust. Inst. 32 (1) (2009) 527–534.

[23] X. Gou, Z. Chen, W. Sun, Y. Ju, A dynamic adaptive chemistry scheme with error control for combustion modeling with a large detailed mechanism, Combust. Flame 160 (2) (2013) 225–231.

[24] H. Yang, Z. Ren, T. Lu, G.M. Goldin, Dynamic adaptive chemistry for turbulent flame simulations, Combust. Theory Model. 17 (1) (2013) 167–183.

[25] Y. Shi, L. Liang, H.-W. Ge, R.D. Reitz, Acceleration of the chemistry solver for modeling DI engine combustion using dynamic adaptive chemistry (DAC) schemes, Combust. Theory Model. 14 (1) (2010) 69–89.

[26] Z. Lu, L. Zhou, Z. Ren, T. Lu, C.K. Law, Effects of spray and turbulence modelling on the mixing and combustion characteristics of an n-heptane spray flame simulated with dynamic adaptive chemistry, flow, Turbul. Combust. 97 (2) (2016) 609–629.

[27] W. Sun, X. Gou, H.A. El-Asrag, Z. Chen, Y. Ju, Multi-timescale and correlated dynamic adaptive chemistry modeling of ignition and flame propagation using a real jet fuel surrogate model, Combust. Flame 162 (4) (2015) 1530–1539.

[28] W. Sun, Y. Ju, Multi-timescale and correlated dynamic adaptive chemistry and transport modeling of flames in n-heptane/air mixtures, 53rd AIAA Aerospace Sciences Meeting (Jan. 2015) 2015-1382, AIAA Paper.

[29] S. Yang, R. Ranjan, V. Yang, S. Menon, W. Sun, Parallel on-the-fly adaptive kinetics in direct numerical simulation of turbulent premixed flame, Proc. Combust. Inst. 36 (2) (2017) 2025–2032.

[30] S. Yang, X. Wang, V. Yang, W. Sun, H. Huo, Comparison of flamelet/progress-variable and finite-rate chemistry LES models in a preconditioning scheme, 55th AIAA Aerospace Sciences Meeting (Jan. 2017) 2017-0605, AIAA Paper.

[31] G.P. Smith, D.M. Golden, M. Frenklach, N.W. Moriarty, B. Eiteneer, M. Goldenberg, C.T. Bowman, R.K. Hanson, S. Song, W.C. Gardiner Jr., V.V. Lissianski, Z. Qin, GRI-Mech 3.0, 1999, http://www.me.berkeley.edu/gri_mech/.

[32] N. Peters, Laminar diffusion flamelet models in non-premixed turbulent combustion, Prog. Energy Combust. Sci. 10 (3) (1984) 319–339.

[33] W.-W. Kim, S. Menon, H.C. Mongia, Large-eddy simulation of a gas turbine combustor flow, Combust. Sci. Technol. 143 (1–6) (1999) 25–62.

[34] W.-W. Kim, S. Menon, Numerical modeling of turbulent premixed flames in the thin-reaction-zones regime, Combust. Sci. Technol. 160 (1) (2000) 119–150.

[35] V. Sankaran, S. Menon, Subgrid combustion modeling of 3-D premixed flames in the thin-reaction-zone regime, Proc. Combust. Inst. 30 (1) (2005) 575–582.

[36] V. Sankaran, S. Menon, LES of scalar mixing in supersonic mixing layers, Proc. Combust. Inst. 30 (2) (2005) 2835–2842.

[37] R.W. MacCormack, The effect of viscosity in hypervelocity impact cratering, J. Spacecr. Rockets 40 (5) (2003) 757–763.

[38] J. Kim, P. Moin, Application of a fractional-step method to incompressible Navier–Stokes equations, J. Comput. Phys. 59 (2) (1985) 308–323.

[39] S. Yang, A. Kurganov, Y. Liu, Well-balanced central schemes on overlapping cells with constant subtraction techniques for the Saint-Venant shallow water system, J. Sci. Comput. 63 (3) (2015) 678–698.

[40] E.P.N. Duque, B.J. Whitlock, S.M. Legensky, C.P. Stone, R. Ranjan, S. Menon, The impact of in situ data processing and analytics upon weak scaling of CFD solvers and workflows, 27th International Conference on Parallel Computational Fluid Dynamics (2015).

[41] P. Brown, G. Byrne, A. Hindmarsh, VODE: a variable-coefficient ODE solver, SIAM J. Sci. Comput. 10 (8) (1989) 1038–1051.

[42] T.R. Bussing, E.M. Murman, Finite-volume method for the calculation of compressible chemically reacting flows, AIAA J. 26 (9) (1988) 1070–1078.

[43] V.R. Katta, W.M. Roquemore, Calculation of multidimensional flames using large chemical kinetics, AIAA J. 46 (7) (2008) 1640–1650.

[44] S. Yang, V. Yang, W. Sun, S. Nagaraja, W. Sun, Y. Ju, X. Gou, Parallel on-the-fly adaptive kinetics for non-equilibrium plasma discharges of $C_2H_4/O_2/Ar$ mixture, 54th AIAA Aerospace Sciences Meeting (Jan. 2016) 2016-0195, AIAA Paper.

[45] V.R. Katta, W.M. Roquemore, Evaluation of kinetics models for JP-8 in predicting unsteady flames, 55th AIAA Aerospace Sciences Meeting (Jan. 2017) 2017-0608, AIAA Paper.

[46] L.K. Su, N.T. Clemens, The structure of fine-scale scalar mixing in gas-phase planar turbulent jets, J. Fluid Mech. 488 (2003) 1–29.

[47] P. Sripakagorn, S. Mitarai, G. Kosály, H. Pitsch, Extinction and reignition in a diffusion flame: a direct numerical simulation study, J. Fluid Mech. 518 (2004) 231–259.

[48] D. Veynante, L. Vervisch, Turbulent combustion modeling, Prog. Energy Combust. Sci. 28 (3) (2002) 193–266.